TWO-DIMENSIONAL SPECTROSCOPY IN SOLID, LIQUID, AND SURFACE

Doctoral Thesis

YUKI NAGATA

Department of Chemistry, Graduate School of Science,
Kyoto University

TABLE OF CONTENTS

ACKNOWLEDGEMENTS

I wish to express my thanks to Prof. Yoshitaka Tanimura in Kyoto University, Prof. Shinji Saito in Institute of Molecular Science (IMS), and Prof. Shaul Mukamel in University of California, Irvine for overall discussions. I also wish to thank Prof. Mark Maroncilli in Wisconsin University for useful comment, Dr. Hisao Nakamura in the University of Tokyo for discussion on surface theory, Dr. Kazuya Watanabe, Prof. Yoshiyasu Matsumoto in IMS, and Dr. Takeshi Yamada in Osaka University on surface experiments. I am grateful to Mr. Yohichi Suzuki, Mr. Taisuke Hasegawa in Kyoto University, Mr. Hitoshi Maruyama in Ricoh Inc., and Dr. Hiroto Kuninaka in Chuo University for much support. Some parts of the numerical calculation were performed at the Computer Center in the IMS.

Chapter 1

OVERVIEWS

1-1. Two-dimensional Raman Spectroscopy

Since the advent of laser technology, optical spectroscopy has moved into a revolutionary new era. Development of nonlinear ultrafast spectroscopy, in particular, has provided exciting new opportunities for researches in a lot of unexplored areas of science and technology. At the same time, the development enables us to perform the new spectroscopic methods. One of these spectroscopic methods is two-dimensional (2D) Raman spectroscopy which is analogous to 2D nuclear magnetic resonance.[1] [2]

2D Raman spectroscopy has been expected to be useful for extracting homogeneous broadening from inhomogeneous broadening.[2] [3] [4] [5] [6] [7] The experiments of 2D Raman spectroscopy, however, were very difficult because their signals were very weak and removing the cascading signal was difficult.[8] The successful demonstration of 2D Raman spectroscopy were done by using CS_2 [9] [10] [11] and benzene [12] both of which have strong polarizabilities.

In spite of these experimental difficulties, theoretical researches have been continued actively because 2D Raman spectroscopy has possibility to reveal the underlying dynamics which cannot be observed in linear Raman spectroscopy. Okumura and Tanimura showed the 2D Raman signal was originated from the nonlinear coordinate dependence of polarizability and anharmonicity of potentials.[13] Saito and Ohmine performed the normal mode calculation of the 2D Raman signals which included only the nonlinear polarizability contributions. However, the anharmonicity of potential contribution was not negligible. Ma and Stratt calculated the 2D Raman signal for Xe from the molecular dynamics (MD) simulations [15] based on a stability matrix formalism.[1] [16] In this method, the fluctuation of polarizability of a system which is related to the 2D Raman response functions via the fluctuation dissipation theorem was calculated.[17] The calculated 2D signals from MD

simulation with the stability matrix formalism [18] reasonably agreed with experimantal results for liquid CS_2 system.[9] On the other hand, 2D Raman signals were calculated from a non-equilibrium MD simulation by Jansen *et al.* in which the laser field was explicitly radiated into the system.[19] [20] [21] In many cases, this non-equilibrium MD method is computationally less expensive than the MD simulation based on the stability matrix formalism. Then, Hasegawa and Tanimura developed a less computationally expensive MD simulation algorism by incorporating the non-equilibrium method into the equilibrium MD method with the fluctuation-dissipation theorem and calculated 2D signals for various liquids.[22]

The approximations to calculate the 2D Raman signal have been also developed. Keyes *et al.* used the Langevin equation formalism.[23] [24] DeVane *et al.* developed the time correlation function theory and applied it to the CS_2 [25] and atomic liquids [26] to calculate the 2D Raman signals. Denny and Reichman used the microscopic molecular hydrodynamics theory for the 2D Raman spectrum of Xe in which the multi-point correlation function was factorized into the products of density correlation functions.[27] [28] The comparison of the results using the microscopic molecular hydrodynamics theory with MD simulation results [15] showed the complete lack of an echo in the hydrodynamic theory. These incomplete descriptions of the 2D Raman signals with these approximated methods may indicate the importance of the multi-point correlation functions and the stability matrix.

Saito and Ohmine investigated the effects of anharmonic dynamics [29] [30] and stability matrix.[29] According to the Okumura and Tanimura's prescription, [13] they focused on t_1 and $t_1 = t_2$ axes for the detection of anharmonic dynamics and stability matrix contributions, respectively. To compare the 2D Raman signal quantitatively, Nagata and Tanimura projected 2D Raman signals to 1D plots without loss of information on the stability matrix using the symmetric and anti-symmetric integrated response functions.[31] They found the dynamics of soft core particles were different for in the liquid phase and in the solid phase even in the ultrafast time scales, which could not be observed in linear Raman spectra. The dynamics was composed of the two modes; one was a localized mode and the other a delocalized mode.[32] These modes were confirmed in the frequency domain 2D Raman maps more clearly than 1D plots.[33] Moreover, they showed that the phase change of the 2D Raman signals was

originated from the nonlinear polarizability contribution rather than anharmonicity contribution, [33] which indicated that the nonlinear polarizability was sensitive to the structural change. Temperature dependence of the 2D Raman spectra was also investigated in the framework of the time correlation function theory.[34]

As we overview these theoretical works on the 2D Raman spectroscopy, it has potentials to investigate the intermolecular interaction and related dynamics in condensed phases through nonlinear polarizability and anharmonic dynamics. Such measurements are, however, difficult and, therefore, new innovations on experimental techniques are called for. Alternatively, some theoretical research themes should be focused on as a target of the 2D Raman spectroscopy. Ionic liquids [35] or liquid mixtures such as water and acetonitrile [36] [37] [38] are interesting systems to carry out the 2D Raman measurements. Although the sensitivity of the 2D Raman spectroscopy to the dynamics between solid and liquid phases was investigated in the present thesis, the sensitivity to the dynamics near the critical temperature is also interesting issue. I believe further researches in such problems make the future of the 2D Raman spectroscopy brilliant.

1-2. Two-dimensional Surface Spectroscopy

The subject of CO bonding and intermolecular dynamics on metal surfaces has attracted considerable attention, with much of the information about the nature of the bond being inferred from measurements of the intramolecular vibrational mode.

As the first stage of theoretical studies, the mechanism of the fast relaxation of the CO stretching mode on metal surfaces was investigated. By using the Anderson model, Persson and Persson showed an electron-hole (e-h) pair creation mechanism contributed to the fast relaxation compared with the phonon effects or the dipole-dipole interactions.[39] e-h pair creation was explained as the action of the induced dipole moments on metal surface caused by the large dynamic dipole moments of CO. The vibrational lifetime estimated was estimated as (3 ± 1) ps, which accords with the experimental results.[40] Head-Gordon and Tully explained the e-h pair creation as a non-adiabatic process. Based on the Fermi's golden rule, they obtained the following expression for the vibrational lifetime

$$\frac{1}{\tau} = \pi\hbar Tr\left[P\left(\varepsilon_F^-\right)GP\left(\varepsilon_F^+\right)G\right], \tag{1.1}$$

where $P\left(\varepsilon_F^-\right)$ and G represented the local density of state below Fermi energy ε_F and scattering matrix, respectively. Equation (1.1) is analogous to Fisher and Lee formula [42] [43] and Seideman and Miller formula.[44] This analogy indicates CO adsorbed on metal surfaces works as the scattering source for free electrons of metal surfaces, because the CO creates discrete energy levels against the continuous energy levels of metal surfaces.[45] Moreover, Head-Gordon and Tully evaluated the vibrational lifetime from the *ab initio* calculation by replacing the $P\left(\varepsilon_F^-\right)$ and $P\left(\varepsilon_F^+\right)$ with the highest occupied molecular orbital (HOMO) and lowest unoccupied molecular orbital (LUMO).[46]

Following these studies, MD simulation in the dilute CO limit was carried out by Tully *et al.*.[47] They treated e-h pair creation as a stochastic process. The residence and random force were calculated from the first principle calculation through Eq. (1.1) and the second fluctuation-dissipation theorem, respectively. They concluded that the relaxation of the CO stretching and CO frustrated rotational modes arose from e-h pair creation, while those of the C-Cu stretching and CO frustrated translational modes were affected by both Cu lattice vibration and e-h pair creation. As the following researches, MD simulations in the medium coverage were performed to investigate the latest coupling between adsorbed molecules on surfaces.[48] [49]

Experimentalists have also made continuous effort to reveal the underlying dynamics caused by the interactions between adsorbed molecules. Interactions between adsorbed molecules play an important role on the geometry and lateral hopping of CO on Pd(100) surface. Moreover, particular attention has been paid to study the overtone and combination bands of CO on Ru(001). Broadening of the overtone frequency of the CO stretch rapidly grows with increasing temperature due to thermally activated decay of two-photon bound state into single phonon states.[50] Large anharmonicities due to lateral coupling lead to the formation of localized two-phonon bound states besides a continuum of delocalized two-phonon states.[51] Investigating the CO-CO interaction is crucial to reveal the underlying mechanism of surface dynamics.

Here, it is hopeful to apply the 2D techniques to surface spectroscopy as the 2D infrared

(IR) spectroscopy has succeeded the direct observation of coupling between different modes. In fact, such new attempts in surface spectroscopies have been actively done for several decades. Guyot-Sionnest combined the photon echo techniques with sum-frequency generation (SFG) [52] [53] to separate the homogeneous linewidth from an inhomogeneous broadening for Si-H vibrations on Si(111) surface.[54] M. Bonn *et al.* determined the intermolecular coupling strength of dipole-coupled CO molecules on Ru(001) using infrared-infrared-visible (IR-IR-VIS) SFG.[55] However, IR-IR-VIS SFG is a third-order nonlinear optical process and is not surface-specific. N. Belabas and M. Joffre demonstrated a visible-infrared 2D spectroscopy in $AgGaS_2$.[56] C. Voelkmann *et al.* combined four-wave mixing with the second-harmonic generation to monitor the temporal evolution of photoexcited one- or two- photon coherence.[57] These experiments have two time intervals between pulses to obtain the information which cannot be accessed by spectroscopies with one time interval.

Nagata and Tanimura investigated the second-order 2D IR surface spectroscopy and revealed the CO latest coupling is dramatically changed by the frustrated rotational mode using MD simulation.[58] The response function in this spectroscopy has the following form.

$$R^{(2)}_{abc}(t_2,t_1)=\left(\frac{i}{\hbar}\right)^2\left\langle\left[\left[\mu_a(t_2),\mu_b(0)\right],\mu_c(-t_1)\right]\right\rangle, \tag{1.2}$$

where $\mu_a(t)$ is the dipole moment at time t in a direction.[1] [59] [60] t_1 and t_2 are the time intervals between first and second interactions with IR pulses and between the second interaction and the detection of the signal, respectively. Since the fifth-order Raman response function

$$R^{(5)}_{abcdef}(t_2,t_1)=\left(\frac{i}{\hbar}\right)^2\left\langle\left[\left[\Pi_{ab}(t_2),\Pi_{cd}(0)\right],\Pi_{ef}(-t_1)\right]\right\rangle \tag{1.3}$$

has the same form as the response function of surface 2D spectroscopy, similar techniques and analyses developed in 2D Raman spectroscopy are expected to be useful in 2D IR surface spectroscopy.[2] [13] [15] [16] [18] [19] [22] [31] [33]

The potentials of these new spectroscopies are not limited to the metal surface but extends from the gas-liquid interfaces,[61] [62] and liquid-solid interfaces [63] to biological system such as membrane systems. Since the signals from the surfaces, however, are weaker than

those form bulk system, multi-dimensional spectroscopies on surfaces may have much difficulties by means of experiments. Nevertheless the author believes the importance and necessity of 2D IR surface spectroscopy will not be faded out.

1-3. Reference

[1] S. Mukamel, *Principles of Nonlinear Optical Spectroscopy* (Oxford University Press, 1995).

[2] Y. Tanimura and S. Mukamel, J. Chem. Phys. **99**, 9496 (1993).

[3] K. Tominaga and K. Yoshihara, Phys. Rev. Lett. **74**, 3061 (1995).

[4] K. Tominaga and K. Yoshihara, J. Chem. Phys. **104**, 4419 (1996).

[5] T. Steffen and K. Duppen, Phys. Rev. Lett. **76**, 1224 (1996).

[6] T. Steffen and K. Duppen, J. Chem. Phys. **106,** 3854 (1997).

[7] A. Tokmakoff and G. R. Fleming, J. Chem. Phys. **106**, 2569 (1997).

[8] D. A. Blank. L. J. Kaufman, and G. R. Fleming, J. Chem. Phys. **111**, 3105 (1999).

[9] L. J. Kaufman, J. Heo, L. D. Ziegler, and G. R. Fleming, Phys. Rev. Lett. **88**, 207402 (2002).

[10] V. Astinov, K. J. Kubarych, C. J. Milne and, R. J. D. Miller, Chem. Phys. Lett. **327**, 34 (2000).

[11] K. J. Kubarych, C. L. Milne, S. Lin, V. Astinov, and R. J. D. Miller, J. Chem. Phys. **116**, 2016 (2002).

[12] C. L. Milne, Y. L. Li, T. l. C. Jansen, L. Huang, and R. J. D. Miller, J. Phys. Chem. B **110**, 19867 (2006).

[13] K. Okumura and Y. Tanimura, J. Chem. Phys.**106**, 1687 (1997).

[14] S. Saito and I. Ohmine, J. Chem. Phys. **108**, 240 (1998).

[15] A. Ma and R. M. Stratt, Phys. Rev. Lett. **85**, 1004 (2000).

[16] S. Mukamel, V. Khidekel, and V. Chernyak, Phys. Rev. E **53**, R1 (1996).

[17] R. Kubo, M. Toda, and N. Hashitsume, *Statistical Physics* 2 (Springer, 1991).

[18] S. Saito and I. Ohmine, Phys. Rev. Lett. **88**, 207401 (2002).

[19] T. l. C. Jansen, J. G. Snijders, and K. Duppen, J. Chem. Phys. **113**, 307 (2000).

[20] T. l. C. Jansen, J. G. Snijders, and K. Duppen, J. Chem. Phys. **114,** 10910 (2001).

[21] T. l. C. Jansen, J. G. Snijders, and K. Duppen,, Phys. Rev. B **67**, 134206 (2003).

[22] T. Hasegawa and Y. Tanimura, J. Chem. Phys. **125**, 074512 (2006).

[23] T. Keyes and J. T. Fourkas, J. Chem. Phys. **112**, 287 (2000).

[24] J. Kim and T. Keyes, Phys. Rev. E **65**, 061102 (2002).

[25] R. DeVane, C. Ridley, B. Space, and T. Keyes, J. Chem. Phys. **119**, 6073 (2003).

[26] R. DeVane, C. Ridley, B. Space, and T. Keyes, J. Chem. Phys. **123**, 194507 (2005).

[27] R. A. Denny and D. R. Reichman, Phys. Rev. E **63**, 065101 (2001).

[28] R. A. Denny and D. R. Reichman, J. Chem. Phys. **116**, 1987 (2002).

[29] S. Saito and I. Ohmine, J. Chem. Phys. **119**, 9073 (2003).

[30] S. Saito and I. Ohmine, J. Chem. Phys. **125**, 084506 (2006).

[31] Y. Nagata and Y. Tanimura, J. Chem. Phys. **124**, 024508 (2006).

[32] H. R. Schober and B. B. Laird, Phys. Rev. B **44**, 6746 (1991).

[33] Y. Nagata, T. Hasegawa, and Y. Tanimura, J. Chem. Phys. **124**, 194504 (2006)

[34] R. DeVane, C. Kasprzyk, B. Space, and T. Keyes, J. Chem. Phys. **123**, 194507 (2005).

[35] H. Shirota, A. M. Funston, J. F. Wishart, and E. W. Castner Jr., J. Chem. Phys. **122**, 184512 (2005).

[36] H. Kano and H. Hamaguchi, J. Chem. Phys. **118**, 4556 (2003).

[37] S. Shigeto, H. Kano, and H. Hamaguchi, J. Chem. Phys. **112**, 064504 (2005).

[38] E. D. Elola and B. M. Ladanyi, J. Chem. Phys. **125**, 184506 (2006).

[39] B. N. J. Persson and M. Persson, Solid State Communications **36**, 175 (1980).

[40] R. Ryberg, Phys. Rev. B **32**, 2671 (1985).

[41] M. H- Gordon and J. C. Tully, J. Chem. Phys. **96**, 3939 (1992).

[42] D. S. Fisher and P. A. Lee, Phys. Rev. B **23**, 6851 (1981).

[43] S. Datta, *Electronic Transport in Mesoscopic Systems* (Cambridge University Press, 1995).

[44] T. Seideman and W. H. Miller in J. Chem. Phys. **96**, 4412 (1992).

[45] H. Nakamura, Private Communication

[46] M. H- Gordon and J. C. Tully, Phys. Rev. B **46**, 1853 (1992).

[47] J. C. Tully, M. Gomez, and M. H- Gordon, J. Vac. Sci. Technol. A **11**, 1914 (1993).

[48] C. Springer, and M. H- Gordon, Chem. Phys. **205**, 73 (1996).

[49] M. -C. Marinica, H. Le Rouzo, and G. Raseev, Surf. Sci. **542**, 1 (2003).

[50] P. Jakob, Phys. Rev. Lett. **77**, 4229 (1996).

[51] P. Jakob and B. N. J. Persson, J. Chem. Phys. **109**, 8641 (1998).

[52] X. D. Zhu and Y. R. Shen, Appl. Phys. B **50**, 535 (1990).

[53] Y. R. Shen, *Principles of Nonlinear Optics* (Willy, 1984).

[54] P. Guyot-Sionnest, Phys. Rev. Lett. **66**, 1489 (1991).

[55] M. Bonn, C. Hess, J. H. Miners, T. F. Heinz, H. J. Bakker, and M. Cho, Phys. Rev. Lett. **86**, 1566 (2001).

[56] N. Belabas and M. Joffre, Opt. Lett. **27**, 2043 (2002).

[57] C. Voelkmann, M. Reichelt, T. Meier, S. W. Koch, and U. Hofer, Phys. Rev. Lett. **92**, 127405 (2004).

[58] Y. Nagata, Y. Tanimura, and S. Mukamel, J. Chem. Phys. *submitted* (2007).

[59] M. Cho, J. Chem. Phys. **112**, 9978 (2000).

[60] R. Venkatramani and S. Mukamel, J. Phys. Chem. B **109**, 8132 (2005).

[61] P. B. Miranda and Y. R. Shen, J. Phys. Chem. B **103**, 3292 (1999).

[62] A. Morita and J. T. Hynes, Chem. Phys. **258**, 371 (2000).

[63] S. Fujiyoshi, T. Ishibashi, and H. Onishi, J. Phys. Chem. B **108**, 10636 (2004).

Chapter 2

TWO-DIMENSIONAL RAMAN SPECTRA OF ATOMIC LIQUIDS AND SOLIDS

2-1. Introduction

One important aspect of molecular vibrational spectroscopies is the ability to monitor ultrafast molecular dynamics controlled by complex inter- and intra-molecular interactions.[1] Vibrational relaxations are in principle dependent upon the configurations of atoms; therefore, we may expect that the information about the local environments of molecules can be obtained by analyzing changes in spectra as functions of conditions such as phase, density, and temperature. However, conventional linear spectroscopy does not reveal such changes because the large broadening caused by damping and inhomogenity makes spectral peaks featureless. To conquer these difficulties, 2D vibrational spectroscopies such as fifth-order Raman spectroscopy [2] [3] [4] and third-order IR spectroscopy [5] have been proposed. In fifth-order Raman spectroscopy a system is perturbed by two pairs of Raman pulses separated by period t_1 and then probed after another period t_2, whereas in the third-order IR spectroscopy a system is perturbed by three IR pulses separated by periods t_1 and t_2 and then probed after another period t_3. These 2D spectroscopies enable us to evaluate the detailed interrogation of the interactions and configurations between molecules, because the contributions to the signals from harmonic vibrational motions vanish in multi-dimensional spectroscopies due to the fact that the Gaussian-integral involves in three-point correlation function, i.e. $\langle[[\Pi(t_1+t_2),\Pi(t_1)],\Pi(0)]\rangle$ for the fifth-order Raman processes and the destructive interferences between vibrational excitations in four-point correlation function, i.e. $\langle[[[\mu(t_1+t_2+t_3),\mu(t_1+t_2)],\mu(t_1)],\mu(0)]\rangle$ for the third-order IR spectroscopy, where $\Pi(t)$ and $\mu(t)$ are a polarizability and a dipole moment at time t. A very large body of theoretical works on 2D Raman and IR spectroscopies have been devoted to the study of

inhomogenity,[1] anharmonicity,[6] [7] [8], and so on. MD simulations have explored ranging from liquids [9] [10] [11] [12] [13] [14] [15] [16] [17] [18] to more complex molecules such as peptides.[19] [20] [21] [22]

2D Raman spectroscopies are advantageous in studying molecular dynamics in condensed phases because Raman pulses can create instantaneous vibrational excitations on the molecular system and their coherence can be detected by spectroscopic means.[23] [24] [25] [26] The sensitivities of the 2D spectra to anharmonicity of the potential and nonlinear dependence of polarizability on nuclear coordinate have been theoretically demonstrated by use of the simple models and have been clarified to some extent with the help of quantum Liouville pathway treatments.[27] [28] [29] But most of these studies have not yet provided helpful pictures of the processes giving rise to particular spectral features in both experimental data and MD simulations. Moreover there has been little guidance from theory on how to distinguish motions of solids and liquids based on these spectroscopies.

In this study, we performed MD simulations to investigate how the fifth-order response functions measured in 2D Raman spectroscopy depended on temperature and thermodynamic state. We have chosen the soft-core model for these simulations because its scaling property allows us to discuss the phase transition as a function of temperature.[30] [31] [32] Note that the soft-core potential has been used to model metallic glasses with soft modes and has been one of the widely acknowledged models explaining so-called “boson peak”.[33] We explored the use of the symmetric and anti-symmetric expressions of the integrated 2D Raman response functions to clarify the interpretation of the spectroscopy data. These functions were originally introduced for an easy check of the simulation results.[34] We then projected the 2D profiles onto two kinds of 1D plots: one is the classical fifth-order response functions on the $t_1=t_2$ axis [16] and the other is the anti-symmetric integrated response function on the $t_1=t_2$ axis. Because these functions can be constructed from experimental data as well as simulation results, they will be valuable for analyzing the effects of nonlinear dynamics, for instance, as result from anharmonicity of the potentials upon the fifth-order signals. The results of our MD simulations indicate that 2D Raman spectroscopy can detect the change in the character of molecular motions in different phases in a way that cannot be observed in third-order Raman spectroscopy. On the other hand, the profile of the 2D Raman signal is not sensitive to

the temperature changes as long as the system is in the same phase. Moreover, when the symmetric integrated response function, which has the form of a simple three-body correlation function, is compared with the anti-symmetric one, with the form of a three-body correlation function including the stability matrix, it is realized what a critical role the stability matrix plays in extracting dynamical information from the fifth-order response function.

In Sec. 2-2, we explain our model and simulation procedures. In Sec. 2-3, we introduce the symmetric and anti-symmetric integrated response functions and in Sec. 2-4 we analyze the calculated signal with these functions. In Sec. 2-5, we discuss the temperature and phase effects on the signals. Finally, Sec. 2-6 is devoted to concluding remarks.

2-2. Computational Details

We perform microcanonical MD simulations with a periodic boundary condition on a system with 108 spheres interacting via a soft potential [33]

$$U(r) = \varepsilon\left(\frac{\sigma}{r}\right)^6 + A\left(\frac{r}{\sigma}\right)^4 + B, \tag{2.1}$$

where ε and σ are the potential parameters, and the constant A and B are chosen to connect the force and potential smoothly at the cutoff r_0. Thus A and B are given by $3/2\cdot\varepsilon(\sigma/r_0)^{10}$ and $-5/2\cdot\varepsilon(\sigma/r_0)^6$, respectively. The molecular system is controlled by laser pulses. The optical response of the system is then described by a correlation function of the polarizability. The total polarizability is treated using a dipole-induced dipole (DID) model, which can be expressed as [35] [36]

$$\Pi(t) = \sum_m \left(\alpha_m - \sum_{n\neq m}\left(\frac{\alpha_m\cdot\alpha_n}{r_{mn}^3(t)} - \frac{3(\alpha_m\cdot\vec{r}_{mn}(t))(\vec{r}_{mn}(t)\cdot\alpha_n)}{r_{mn}^5(t)} \right)\right), \tag{2.2}$$

where α_m is the molecular polarizability of atom m. The second term is important because it possesses the information on the configuration of the surrounding particles. The third- and fifth-order response functions, $R^{(3)}_{abcd}(t_1)$ and $R^{(5)}_{abcdef}(t_2,t_1)$, which are associated with the 1D and 2D Raman spectroscopy, respectively, are given as follows.[1]

$$R^{(3)}_{abcd}(t_1) = \frac{i}{\hbar}\left\langle\left[\Pi_{ab}(t_1), \Pi_{cd}(0)\right]\right\rangle, \tag{2.3}$$

$$R^{(5)}_{abcdef}(t_2, t_1) = \left(\frac{i}{\hbar}\right)^2 \left\langle\left[\left[\Pi_{ab}(t_2), \Pi_{cd}(0)\right], \Pi_{ef}(-t_1)\right]\right\rangle, \tag{2.4}$$

where $\Pi_{ab}(t)$ is the *ab* tensor element of the polarizability at time *t*, $\left[\hat{A}, \hat{B}\right] \equiv \hat{A}\hat{B} - \hat{B}\hat{A}$ is the quantum commutator, and $\langle\cdots\rangle$ is an ensemble average over an equilibrium initial distribution. In the classical limit, the operators $\hat{E}$ and $\hat{F}$ commute with $\mathrm{e}^{\lambda\hat{H}}$ and we have [10]

$$R^{(3)}_{abcd}(t_1) = -\beta\left\langle\dot{\Pi}_{ab}(t_1)\Pi_{cd}(0)\right\rangle, \tag{2.5}$$

$$\begin{aligned} R^{(5)}_{abcdef}(t_2, t_1) &= \beta^2\left\langle\Pi_{ab}(t_2)\dot{\Pi}_{cd}(0)\dot{\Pi}_{ef}(-t_1)\right\rangle \\ &\quad - \beta\left\langle\Pi_{ab}(t_2)\left\{\Pi_{cd}(0), \dot{\Pi}_{ef}(-t_1)\right\}_{P.B.}\right\rangle, \\ &= -\beta\left\langle\left\{\Pi_{ab}(t_2), \Pi_{cd}(0)\right\}_{P.B.}\dot{\Pi}_{ef}(-t_1)\right\rangle \end{aligned} \tag{2.6}$$

where $\{\cdots\}_{P.B.}$ denotes the Poisson bracket producing stability matrices $\partial p_k(t_2)/\partial q_l(0)$ representing how large the deviation of the momentum of atom *k* at time t_2 is caused by the slight displacement of atom *l* at time 0.[37] The significance of the fifth-order measurement arises from the correlation function including the stability matrix, since the stability matrix carries the information on the interference of the particle trajectories that cannot be obtained from the third-order measurement.

There are two approaches to evaluate these signals using MD simulations, the equilibrium approach [11] [15] [16] and the no-equilibrium approach.[13] [14] [16] Here we adopt the former, because it best reveals the importance of the stability matrix to determine the nature of the fifth-order Raman response. In the stability matrix approach, we first carry out the equilibrium simulation, then evaluate the response function using the trajectories of particles obtained from the simulations.

To perform the simulation, we set $\varepsilon = 1.0$, $\sigma = 1.0$, and $m = 1.0$ without loss of generality, where *m* is the particle mass. Because of the scaling property of the soft-core potential, a temperature times the Boltzmann constant, *kT*, is chosen as a parameter with fixed density $\rho = 1.0$. We use a fourth-order symplectic integrator method with a time step of 0.01. The particles form an face-centered cubic (fcc) lattice for $kT \le 0.19$, and they behave like

liquid for $0.19 \le kT$. There is also a body-centered cubic (bcc) phase around $kT \approx 0.19$, but the region of this phase is relatively narrow.[31] [32] Here we calculate the third- and fifth-order response functions in the fcc solid and liquid phases. The MD simulations start from an fcc configuration with double the targeted temperature and cools the system by velocity rescaling at the rate of 0.002 for each time step. After the kinetic energy of the system reaches *kT*=0.001, we heat the system up to the targeted temperature. In both cases, we sample over 60,000 trajectories by preparing different initial configurations to calculate the response functions, and we use more than 3500 time steps to stabilize the kinetic energy. As the polarizability is independent of momentum, only $\partial\vec{p}(t_2)/\partial\vec{q}(t_1)$ of the stability matrix element is calculated, which decreases to one-fourth the computational cost of evaluating the full stability matrices and reduces the memory requirements for sampling trajectories.

2-3. Fifth-order Symmetric and Antisymmetric Integrated Response Functions

As has been shown in many previous studies, the 2D profiles of the fifth-order Raman signals are very sensitive to the anharmonicity of the molecular dynamics and nonlinear dependence of the polarizability. But interpreting the 2D profiles in terms of the underlying dynamics is difficult due to the complex connection between the dynamics and spectroscopy. Since the most significant and interesting contribution to the fifth-order signals comes from the term with the stability matrix,[16] it is valuable and versatile if we can separate it from the others. For this purpose, we utilize the symmetric integrated response function introduced by Cao *et al*.[34] and the anti-symmetric integrated response function.

To simplify the following explanation, we choose *z* direction for all tensors and afterward we omit the tensor notation. To make the symmetric form with respect to t_1 and t_2 from the fifth-order response function, we integrate Eq. (2.6) with respect to t_1,

$$\begin{aligned} W(t_2,t_1) &\equiv \frac{1}{\beta}\int_0^{t_1} R^{(5)}(t_2,t')dt' \\ &= -\beta\left[\left\langle \Pi(t_2)\dot{\Pi}(0)\Pi(-t_1)\right\rangle - \left\langle \Pi(t_2)\dot{\Pi}(0)\Pi(0)\right\rangle\right] + \left\langle \Pi(t_2)\{\Pi(0),\Pi(-t_1)\}_{P.B.}\right\rangle . \\ &= \left\langle \{\Pi(t_2),\Pi(0)\}_{P.B.}\Pi(-t_1)\right\rangle - \left\langle \{\Pi(t_2),\Pi(0)\}_{P.B.}\Pi(0)\right\rangle \end{aligned} \qquad (2.7)$$

Then, by using the relations

$$\frac{1}{\beta}\int_0^\infty R^{(5)}(t_2,t')dt' = \beta\left\langle \Pi(t_2)\dot{\Pi}(0)\Pi(0)\right\rangle = -\left\langle \{\Pi(t_2),\Pi(0)\}_{P.B.}\Pi(0)\right\rangle, \tag{2.8}$$

and

$$\left\langle \{\Pi(t_1),\Pi(0)\}_{P.B.}\Pi(-t_2)\right\rangle = \left\langle \Pi(t_2)\{\Pi(0),\Pi(-t_1)\}_{P.B.}\right\rangle, \tag{2.9}$$

we have the symmetric integrated response functions as

$$\begin{aligned} S(t_2,t_1) &\equiv W(t_2,t_1) - W(t_1,t_2) \\ &= \beta\left\langle \Pi(t_2)\dot{\Pi}(0)\Pi(-t_1)\right\rangle + \beta\left\langle \Pi(t_2)\dot{\Pi}(0)\Pi(0)\right\rangle - \beta\left\langle \Pi(0)\dot{\Pi}(0)\Pi(-t_1)\right\rangle \end{aligned}. \tag{2.10}$$

Here, we also introduce its counterpart, the anti-symmetric integrated response function,

$$\begin{aligned} A(t_2,t_1) &\equiv W(t_2,t_1) + W(t_1,t_2) \\ &= \left\langle \Pi(t_2)\{\Pi(0),\Pi(-t_1)\}_{P.B.}\right\rangle - \left\langle \Pi(0)\{\Pi(0),\Pi(-t_1)\}_{P.B.}\right\rangle \\ &\quad + \left\langle \{\Pi(t_2),\Pi(0)\}_{P.B.}\Pi(-t_1)\right\rangle - \left\langle \{\Pi(t_2),\Pi(0)\}_{P.B.}\Pi(0)\right\rangle \end{aligned}. \tag{2.11}$$

Although no special attention has previously been paid to the anti-symmetric integrated response function, we find that it contains the key to analyze liquid dynamics because it isolates the contribution of the stability matrix from that of the simple three-point correlation function. In the following, we demonstrate this point by using the present model in the solid and liquids phases. If the above expressions are described with the normal mode, the last two terms in Eqs. (2.10) and (2.11) negate with the terms such as $\Pi'\Pi'\Pi$ (see Eq. (23)). Thus, the leading terms of the symmetric and anti-symmetric integrated response functions both involve $\Pi''\Pi'\Pi'$.

As is evident from the definition, these functions satisfy the relations,

$$S(t_2,t_1) = -S(t_1,t_2), \tag{2.12}$$

and

$$A(t_2,t_1) = A(t_1,t_2). \tag{2.13}$$

Moreover, the functions are orthogonal to one another,

$$\iint dt_1 dt_2 A(t_2,t_1)\cdot S(t_2,t_1) = 0, \tag{2.14}$$

which indicates the information of the symmetric integrated response functions is independent of that of the anti-symmetric ones.

The symmetric integrated response function $S(t_2,t_1)$ is useful for self-consistent checks of numerical simulations,[34] because it does not involve the stability matrix and its numerical

calculation is $1/N^2$ times faster than that of the full fifth-order response function. On the contrary, calculation of the anti-symmetric integrated response function, $A(t_2,t_1)$, requires the same cost as calculation of the fifth-order response function. But it contains the important information on coherent molecular motions described by the stability matrix. It is of importance to notice that although the present analysis is based on the MD simulation, one can also construct the symmetric and anti-symmetric integrated response functions from experimental data. By utilizing these functions, one can quantitatively discuss the effects of nonlinear dynamics, for instance, from anharmonicity.

To illustrate the nature of these functions, we calculate them from the soft-core model in the solid and liquid phases. In Fig. 2.1, we plot the fifth-order response function $R^{(5)}(t_2,t_1)$, the symmetric and anti-symmetric integrated response functions $S(t_2,t_1)$ and $A(t_2,t_1)$, and the derivatives of $S(t_2,t_1)$ and $A(t_2,t_1)$ with respect to t_1,

$$R_S^{(5)}(t_2,t_1) \equiv \partial S(t_2,t_1)/\partial t_1 , \tag{2.15}$$

and

$$R_A^{(5)}(t_2,t_1) \equiv \partial A(t_2,t_1)/\partial t_1 , \tag{2.16}$$

for kT=0.155 in the solid phase. To compare the contributions of the symmetric and anti-symmetric components of the fifth-order response function, in Fig. 2.2 we plot the diagonal slices $R^{(5)}(t,t)$, $R_S^{(5)}(t,t) \equiv \partial S(t_2,t_1)/\partial t_1\big|_{t=t_1=t_2}$, and $R_A^{(5)}(t,t) \equiv \partial A(t_2,t_1)/\partial t_1\big|_{t=t_1=t_2}$ of $R^{(5)}(t_2,t_1)$, $R_S^{(5)}(t_2,t_1)$, $R_A^{(5)}(t_2,t_1)$. Notice that $R^{(5)}(t_2,t_1) = R_S^{(5)}(t_2,t_1) + R_A^{(5)}(t_2,t_1)$.

The position of the peak appearing in $R^{(5)}(t_2,t_1)$ is not necessarily located on the t_1=t_2 axis. In fact, we can estimate the peak position in Fig. 2.1(a) is $(t_2,t_1) = (0.77,0.64)$ by using a parabolic interpolation. Analyzing the fifth-order signals is difficult because 2D profiles of the signals are usually featureless and the locations of their peaks do not necessarily correspond to specific physical processes. Although the profiles can be changed with the physical conditions, it is very hard to choose portions of the 2D signals to make comparisons. Since the anti-symmetric integrated response function always exhibits a symmetric peak along t_1=t_2 axis and is sensitive to the physical conditions due to the contribution from the stability matrix term, it is more instructive to analyze the signals using it instead of the fifth-order response function. In the following, we discuss the parameter dependences of the 2D Raman signals with the help of the anti-symmetric integrated response function.

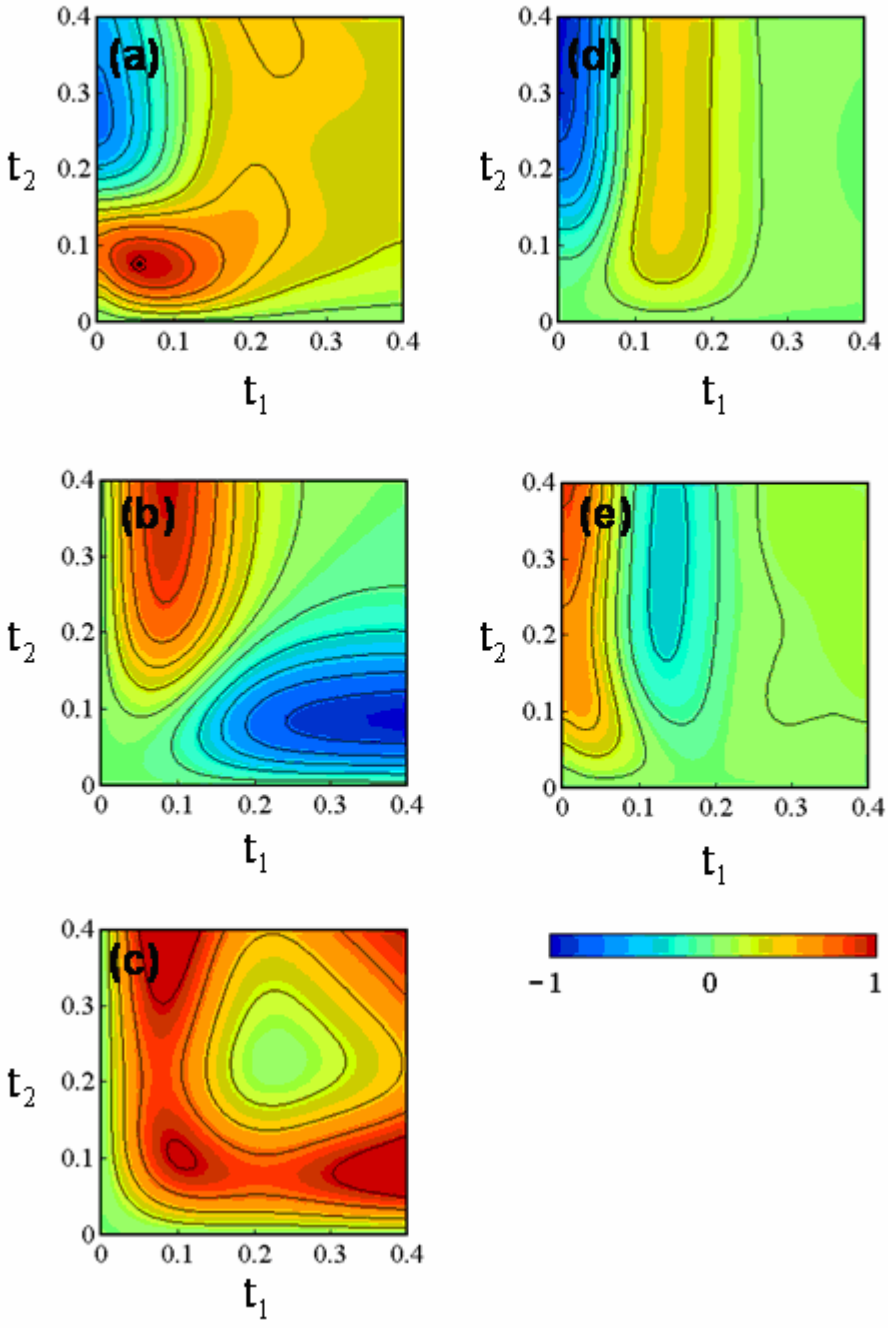

Figure 2.1. (a) $R^{(5)}(t_2,t_1)$, (b) $S(t_2,t_1)$, (c) $A(t_2,t_1)$, (d) $R_S^{(5)}(t_2,t_1)$, and (e) $R_A^{(5)}(t_2,t_1)$ at kT=0.155 in the solid phase. The peak position at $(t_2,t_1)=(0.77,0.64)$ is denoted by a double circle in Fig. 1(a).

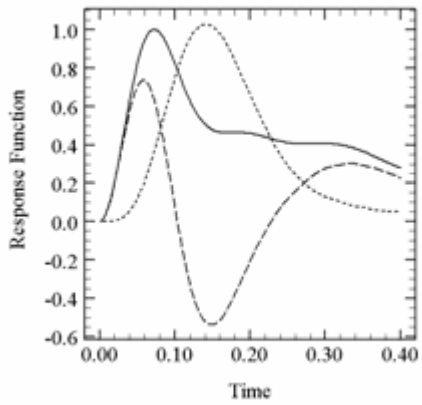

Figure 2.2; Diagonal slices (t=t_1=t_2) from the signals depicted in Fig. 2.1: $R^{(5)}(t,t)$ (solid curve), $R_S^{(5)}(t,t)$ (dotted), and $R_A^{(5)}(t,t)$ (dashed).

2-4. Symmetric and Antisymmetric Integrated Response Function for Normal Mode Analysis

In a normal mode analysis, molecular motions are represented by an ensemble of oscillatory motions along the nuclear coordinates.[1] [38] [39] [40] This analysis is often useful since it gives us access to the microscopic dynamics related to a specific vibrational frequency.[41] Since the fifth-order experiments have the ability to measure anharmonic vibrational motions through the stability matrix term, it is interesting to observe how the symmetric and anti-symmetric integrated response functions contribute to the signals in the normal mode analysis.

When the polarizability is given in powers of a molecular coordinate as

$$\Pi(t)=\Pi(0)+\Pi'(q(t)-q(0))+\frac{1}{2}\Pi''(q(t)-q(0))^2+\cdots, \tag{2.17}$$

the third- and fifth-order response functions $R^{(3)}(t_1)$ and $R^{(5)}(t_2,t_1)$ can be expressed as

$$R^{(3)}(t_1)=\langle\Pi'\Pi'C''(t_1)\rangle\propto\int d\omega\rho(\omega)\frac{\sin(\omega t_1)}{\omega}, \tag{2.18}$$

$$\begin{aligned}R^{(5)}(t_2,t_1)&=\langle\Pi''\Pi'\Pi'C''(t_2)(C''(t_1)+C''(t_1+t_2))\rangle\\&\propto\int d\omega\rho(\omega)\frac{\sin(\omega t_2)(\sin(\omega t_1)+\sin(\omega(t_1+t_2)))}{\omega^2},\end{aligned} \tag{2.19}$$

where $C''(t) = \sin(\omega t)/\omega$. We then obtain the following results on $t=t_1=t_2$,

$$S(t,t) = 0, \tag{2.20}$$

$$A(t,t) \propto \int d\omega \rho(\omega) \frac{\sin^3(\omega t)}{\omega^3}. \tag{2.21}$$

Since $S(t,t)$ gives zero, we substitute $R_S^{(5)}(t,t)$ and $R_A^{(5)}(t,t)$ for $S(t,t)$ and $A(t,t)$,

$$R_S^{(5)}(t,t) \propto \int d\omega \rho(\omega) \frac{\sin^2(\omega t)(1-\cos(\omega t))}{\omega^2}, \tag{2.22}$$

$$R_A^{(5)}(t,t) \propto \int d\omega \rho(\omega) \frac{\sin^2(\omega t)\cos(\omega t)}{\omega^2}. \tag{2.23}$$

$R^{(5)}(t,t)$, $R_S^{(5)}(t,t)$, and $R_A^{(5)}(t,t)$ can be expressed in terms of $R^{(3)}(t)$ as

$$R^{(5)}(t,t) \propto \int_0^t dt\left(6R^{(3)}(3t) + 4R^{(3)}(2t) - 2R^{(3)}(t)\right), \tag{2.24}$$

$$R_S^{(5)}(t,t) \propto \int_0^t dt\left(-3R^{(3)}(3t) + 4R^{(3)}(2t) + R^{(3)}(t)\right), \tag{2.25}$$

$$R_A^{(5)}(t,t) \propto \int_0^t dt\left(9R^{(3)}(3t) - 3R^{(3)}(t)\right). \tag{2.26}$$

Thus, by comparing $R_S^{(5)}(t,t)$ and $R_A^{(5)}(t,t)$ calculated from the fifth-order response functions with $\int_0^t dt\left(-3R^{(3)}(3t) + 4R^{(3)}(2t) + R^{(3)}(t)\right)$ and $\int_0^t dt\left(9R^{(3)}(3t) - 3R^{(3)}(t)\right)$, we can easily estimate the contribution from the anharmonic dynamical terms resulting from the stability matrix and the validity of the normal mode expressions. In Fig. 2.3, we compare $R^{(5)}(t,t)$, $R_S^{(5)}(t,t)$, and $R_A^{(5)}(t,t)$ with their expressions in terms of $R^{(3)}(t)$ under the normal mode assumption. Figure 2.3(a) clearly shows us that the normal mode expressions fail to predict the fifth-order response functions even in the short time region. However, if we focus on Fig. 2.3(b), we see that the normal mode expressions for the symmetric integrated response functions are valid in the region $t \le 0.10$. The normal mode analysis can describe the accurate dynamics in the short time, which is consistent with the results of the symmetric integrated response functions. One of the reasons for the large deviation at $t \ge 0.10$ can be deduced from Brownian motion theory. When the function $C''(t)$ is expressed by

$$C''(t) = \frac{1}{\sqrt{\omega^2 - \zeta^2/4}} e^{-\zeta t/2} \sin\left(\sqrt{\omega^2 - \zeta^2/4}\, t\right) \tag{2.27}$$

in the Brownian oscillator model, the quantities calculated from the fifth-order response function decay more rapidly than the predictions using the third-order response function. On the other hand, in Fig. 2.3(c), $R_A^{(5)}(t,t)$ deviates from $\int_0^t dt\left(9R^{(3)}(3t) - 3R^{(3)}(t)\right)$ even for $t \le 0.10$, which indicates that the anharmonic contribution from the stability matrix $\langle \Pi'\Pi'\Pi'(\partial q(t_2)/\partial p(0))\dot{q}(-t_1)\rangle$ plays an important part in the anti-symmetric integrated response function. Moreover the deviation of the fifth-order response function from the normal mode expression shown in Fig. 2.3(a) is mainly caused by the anti-symmetric part.

2-5. Temperature Dependence

We discuss the response functions in the solid and liquid phases at different temperatures. In Fig. 2.4(a), we depict the third-order response functions $R^{(3)}(t)$ for *kT*=0.215 and 0.20 in the liquid phases and for *kT*=0.155 and 0.14 in the solid phases.[42]

The profiles of the third-order signals in Fig. 2.4 are similar but their decay times are slightly different for different temperature.[43] The fifth-order response functions $R^{(5)}(t_2, t_1)$ are shown in Fig. 2.5. To illustrate the difference between solid and liquid phases, we also plot $R^{(5)}(t,t)$ for different temperatures as 1D maps in Fig. 2.6. There are differences between Figs. 2.5(a), (b) in the liquid phases, and (c), (d) in the solid phases for $t_1 \ge 0.2$ and $t_2 \ge 0.2$. Figure 2.6 clearly shows that the phase change leads to a change of the spectral decay rates especially for $t \ge 0.15$, while the temperature change has a limited effect as long as the system is in the same phase.

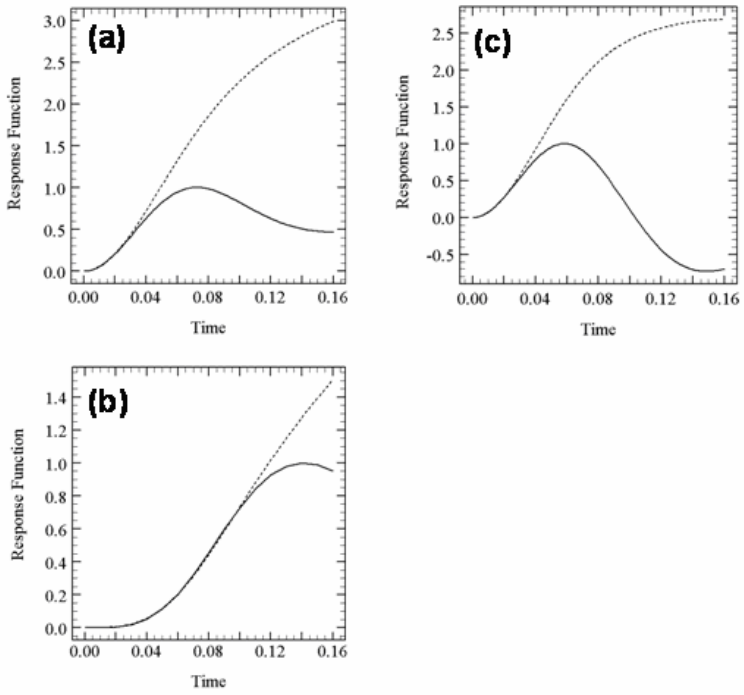

Figure 2.3. (a) $R^{(5)}(t,t)$ (solid line) and $\int_0^t dt\left(6R^{(3)}(3t)+4R^{(3)}(2t)-2R^{(3)}(t)\right)$ (dotted line), (b) $R_S^{(5)}(t,t)$ (solid line) and $\int_0^t dt\left(-3R^{(3)}(3t)+4R^{(3)}(2t)+R^{(3)}(t)\right)$ (dotted line), and (c) $R_A^{(5)}(t,t)$ (solid line) and $\int_0^t dt\left(9R^{(3)}(3t)-3R^{(3)}(t)\right)$ (dotted line) at kT=0.155 in the solid phase. In each figure, the intensities of the solid lines are normalized at the first peak and the dotted lines are scaled so that their derivatives are same as those of solid lines near t=0.

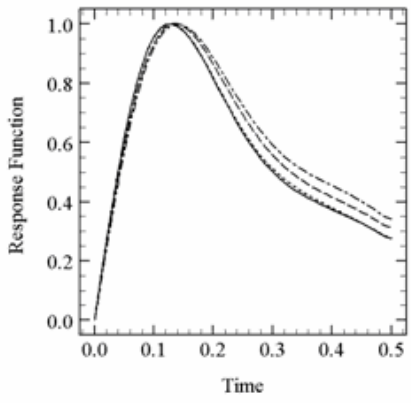

Figure 2.4. The third-order response functions $R^{(3)}(t)$ are depicted for kT=0.215 (solid line), 0.20 (dotted line) in liquid phases, and kT=0.155 (dashed line), 0.14 (dot-dash line) in solid phases. The intensities are normalized.

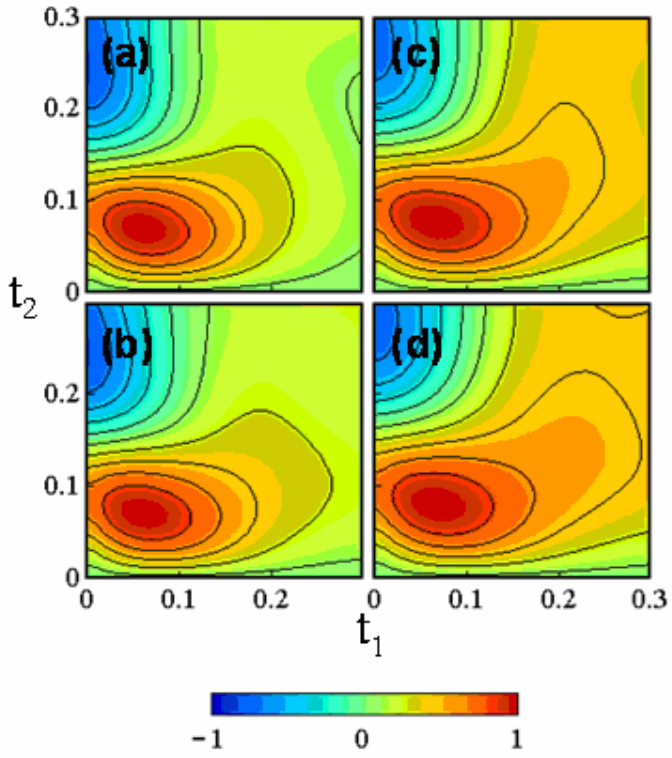

Figure 2.5. The classical fifth-order response functions $R^{(5)}(t_2, t_1)$ for the cases (a) kT=0.215, (b) kT=0.20 in the liquid phase, and (c) kT=0.155, (d) kT=0.14 in the solid phase. The intensity of each plot is normalized at the first peak.

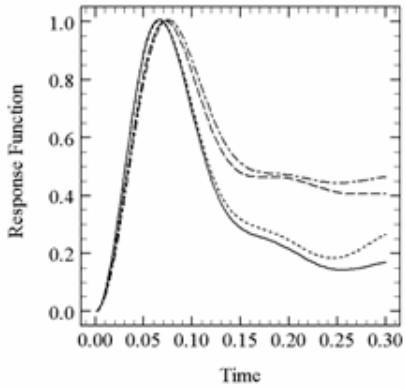

Figure 2.6. The diagonal elements, $R^{(5)}(t,t)$, are illustrated for kT=0.215 (solid line), 0.20 (dotted line) in the liquid phase, and kT=0.155 (dashed line), 0.14 (dot-dash line) in the solid phase. The intensity of each plot is normalized at the first peak.

Although we can observe differences in the fifth-order response functions between different phases, it is more convenient to employ the symmetric integrated response function $S(t_2,t_1)$ and the anti-symmetric one $A(t_2,t_1)$ so as to see the effects of the stability matrices. In Figs. 2.7 and 8, we depict these functions. The diagonal elements of the anti-symmetric integrated response functions $A(t,t)$ are also plotted in Fig. 2.9. While we observe similar tendencies among the results of $S(t_2,t_1)$ in Figs. 2.7(a)-(d), we see the clear difference among the results of $A(t_2,t_1)$ in the liquid and solid phases in Figs. 2.8(a)-(d) in $t_1 \geq 0.2$ and $t_2 \geq 0.2$ and Fig. 2.9 in $t \geq 0.15$. Although we cannot do longer simulations due to the limitations to our computational power, we may expect the bigger and clearer differences in the decay rates in the anti-symmetric response functions appear in the longer time region. The sensitivity of $A(t_2,t_1)$ and insensitivity of $S(t_2,t_1)$ to the phase change result from the stability matrix which reveals deviations from harmonic motion as the interference between the trajectories. The anti-symmetric integrated response functions, which can be obtained from experimental data as well as simulation results by following the procedure explained in Sec. 2-3, are more valuable than the symmetric ones, because the former allow us to estimate the contribution from the stability matrix directly.

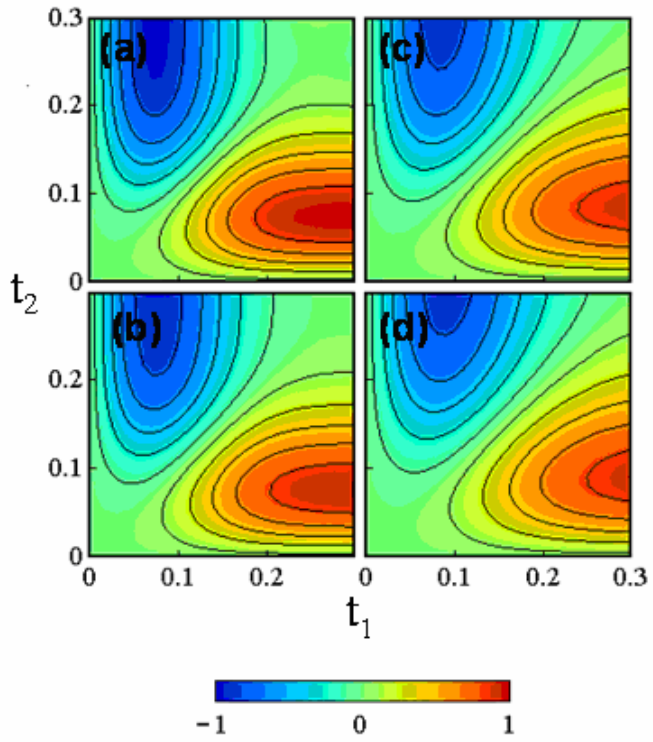

Figure 2.7. The symmetric integrated response functions $S(t_2, t_1)$ are plotted as 2D contour maps for the cases (a) at *kT*=0.215, (b) at *kT*=0.20 in liquid phase, and (c) at *kT*=0.155, (d) at *kT*=0.14 in solid phase. The intensity of each figure is normalized at the first peak.

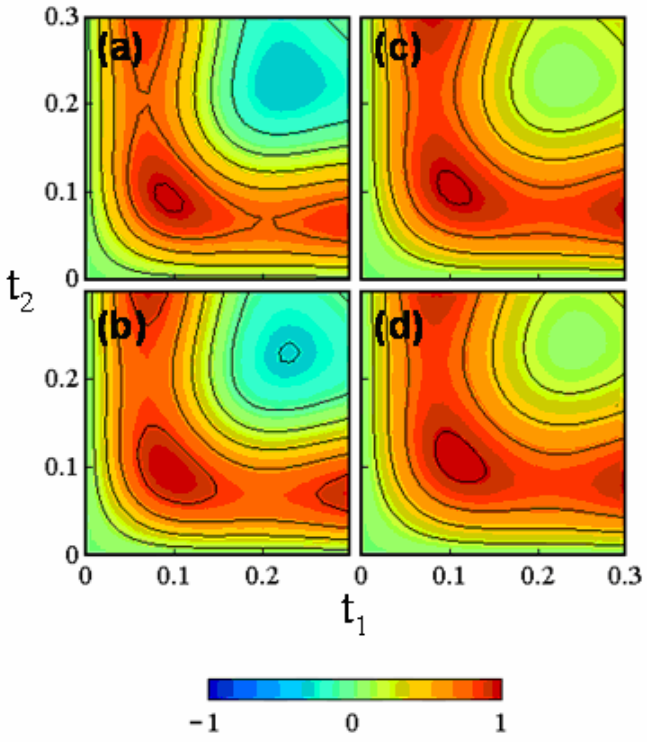

Figure 2.8. The differences of the anti-symmetric integrated response functions $A(t_2,t_1)$ are plotted as two-dimensional contour maps for the cases (a) at kT=0.215, (b) at kT=0.20 in liquid phase, and (c) at kT=0.155, (d) at kT=0.14 in solid phase. The intensity of each plot is normalized at the first peak.

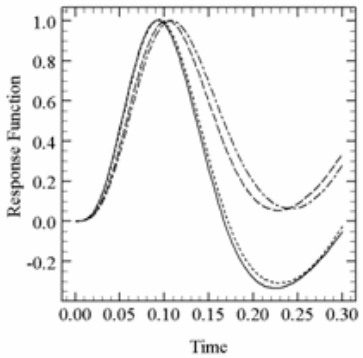

Figure 2.9. The diagonal elements $A(t,t)$ are illustrated for kT=0.215 (solid line), 0.20 (dotted line) in liquid phase, and kT=0.155 (dashed line), 0.14 (dot-dash line) in solid phase. The intensity of each plot is normalized at the first peak.

2-6. Conclusion

Using the MD simulation, we calculated the third- and fifth-order Raman signals of atomic solids and liquids described by the soft-core potential. To analyze these signals quantitatively and to reveal the effect of the stability matrix, we have decomposed the classical fifth-order response function into the symmetric and anti-symmetric integrated response functions; the symmetric one has the form of the simple three-body correlation function, while the anti-symmetric one also includes contributions from the stability matrix. The latter can not be expressed accurately in terms of normal modes expressions even in the short time region, where the symmetric integrated response function can be. This fact indicates that the anharmonic contributions which are missing in the normal mode expressions give rise to an important effect on the fifth-order signals.

It is shown that the change between liquid and solid phases causes a minor effect on the third-order signals, while it causes dramatic differences in the fifth-order signals. The anti-symmetric integrated response functions show prominent changes as a result of the phase transition, whereas the change in the symmetric one is modest. The difference between the symmetric and anti-symmetric integrated response functions results from the sensitivity of the stability matrix to the nonlinear dynamics, because the stability matrix reveals the deviation from the harmonic motion as the interference between the trajectories. This result suggests the advantage of using the anti-symmetric integrated response functions rather than the fifth-order response functions for analysis. Such features are, however, unable to be revealed within the frame work of the normal mode analysis, since it neglects the effects from the anharmonicity described by the stability matrix.

Since we can always construct the symmetric and anti-symmetric integrated response functions not only from the simulation results but also from the experimental data, these functions will be valuable and versatile tools for analyzing the effects of nonlinear dynamics upon the fifth-order signals.

2-7. Reference

[1] Y. Tanimura and S. Mukamel, J. Chem. Phys. **99**, 9496 (1993).

[2] V. Astinov, K. J. Kubarych, C. J. Milne and, R. J. D. Miller, Chem. Phys. Lett. **327**, 34 (2000).

[3] K. J. Kubarych, C. L. Milne, S. Lin, V. Astinov, and R. J. D. Miller, J. Chem. Phys. **116**, 2016 (2002).

[4] L. J. Kaufman, J. Heo, L. D. Ziegler, and G. R. Fleming, Phys. Rev. Lett. **88**, 207402 (2002).

[5] P. Hamm, M. Lim and R. M. Hochstrasser, J. Phys. Chem. B **102**, 6123 (1998)

[6] K. Okumura and Y. Tanimura, J. Chem. Phys.**106**, 1687 (1997).

[7] Y. Tanimura, Chem. Phys. **233**, 217 (1998).

[8] R. B. Williams and R. F. Loring, J. Chem. Phys. **113**, 1932 (2000).

[9] S. Ryu and R. M. Stratt, J. Phys. Chem. B **108**, 6782 (2004).

[10] S. Saito and I. Ohmine, J. Chem. Phys. **108**, 240 (1998).

[11] A. Ma and R.M. Stratt, Phys. Rev. Lett. **85**, 1004 (2000)

[12] A. Ma and R.M. Stratt, J. Chem. Phys. **116**, 4972 (2002).

[13] T. l. C. Jansen, J. G. Snijders, and K. Duppen, J. Chem. Phys. **113**, 307 (2000)

[14] T. l. C. Jansen, J. G. Snijders, and K. Duppen, J. Chem. Phys. **114,** 10910 (2001).

[15] S. Saito and I. Ohmine, Phys. Rev. Lett. **88**, 207401 (2002).

[16] S. Saito and I. Ohmine, J. Chem. Phys. **119**, 9073 (2003).

[17] A. Piryatinski and J. L. Skinner, J. Phys. Chem. B **106**, 8055 (2002)

[18] C. P. Lawrence and J. L. Skinner, J. Chem. Phys. **119**, 3840 (2003).

[19] K. Kwac, H. Lee, and M. Cho, J. Chem. Phys. **120**, 1477 (2004).

[20] K. A. Merchant, W. G. Noid, D. E. Thompson, R. Akiyama, R. F. Loring, and M. D. Fayer, J. Phys. Chem. B **107**, 4 (2003).

[21] A. M. Moran, S. -M. Park, and S. Mukamel, J. Chem. Phys. **118**, 9971 (2003).

[22] T. Hayashi and S. Mukamel, J. Phys. Chem. A **107**, 9113 (2003).

[23] S. Mukamel, V. Khidekel, and V. Chernyak, Phys. Rev. E **53**, R1 (1996).

[24] M. Cho, *Two-dimensional vibrational spectroscopy, in Advances in Multi-photon Process and Spectroscopy*, ed. S.H. Lin, A.A. Villaeys and Y. Fujimura, (World

Scientific, Singapore, 1999), vol. 12, p. 229.

[25] S. Mukamel, Annu. Rev. Phys. Chem. **51**, 691 (2000).

[26] J. T. Fourkas, Adv. Chem. Phys. **117**, 235 (2001).

[27] T. Steffen, J. T. Fourkas, and K. Duppen, J. Chem. Phys. **105**, 7364 (1996).

[28] K. Okumura and Y. Tanimura, J. Phys. Chem. A **107**, 8092 (2003).

[29] W. G. Noid and R. F. Loring, J. Chem. Phys. **121**, 7057 (2004).

[30] W. G. Hoover, S. G. Gray, and K. W. Johnson, J. Chem. Phys. **55,** 1128 (1971).

[31] W. G. Hoover, D. A. Young, and R. Grover, J. Chem. Phys. **56**, 2207 (1972).

[32] B. B. Laird and A. D. J. Haymet, Mol. Phys. **75**, 71 (1992).

[33] H. R. Schober and B. B. Laird, Phys. Rev. B **44**, 6746 (1991).

[34] J. Cao, S. Yang, and J. Wu, J. Chem. Phys. **116**, 3760 (2002).

[35] P. A. Madden and D. J. Tildesley, Mol. Phys. **55**, 969 (1985).

[36] B. M. Ladanyi, Chem. Phys. Lett. **121**, 351 (1985).

[37] S. Mukamel, V. Khidekel, and V. Chernyak, Phys. Rev. E **53**, R1 (1996).

[38] M. Buchner, B.M. Ladanyi, and R.M. Stratt, J. Chem. Phys. **97**, 8522 (1992).

[39] R.M. Stratt and M.H. Cho, J. Chem. Phys. **100**, 6700 (1994). 2

[40] R.M. Stratt, Acc. Chem. Res. **28**, 201 (1995).

[41] M. Cho, G.R. Fleming, S. Saito, I. Ohmine, and R.M. Stratt, J. Chem. Phys. **100**, 6672 (1994).

[42] Since we consider a small system of 108 particles in the present simulations, there are large fluctuations of temperature. These fluctuations cause the difficulty in carrying out the simulation near the phase transition temperature kT=0.19 because during the simulation the molecular states may take both solid and liquid phases due to the fluctuation of the temperature. Therefore, we avoid the regions at near kT=0.19 in our simulations.

[43] K. Okumura, B. Bagchi, and Y. Tanimura, Bull. Chem. Soc. Jpn. **73**, 873 (2000).

Chapter 3

ANALYZING ATOMIC LIQUIDS AND SOLIDS: TWO-DIMENSIONAL RAMAN SPECTRA IN FREQUENCY DOMAIN

3-1. Introduction

Nonlinear optical interactions between the laser and molecular system provide valuable and versatile spectroscopic information to understand the dynamics of the system as well as its environment. For molecules in a condensed phase, fifth-order Raman and third-order IR spectroscopies allow us to capture greater details in molecular dynamics and structure than third-order Raman and first-order IR spectroscopies.[1] The utility and possibility of these spectroscopies have been demonstrated by various approaches including theoretical analyses,[2] [3] MD simulations,[4] [5] [6] [7] [8] [9] [10] [11] [12] [13] [14] [15] [16] [17] [18] [19] [20] *ab initio* calculations,[21] [22] [23] [24] and a variety of experiments.[25] [26] [27] [28] [29] [30] [31] [32] [33] Although the potential of multi-dimensional vibrational spectroscopies is now well recognized, our comprehension of 2D contour maps has not been achieved completely. In a fifth-order Raman case, this might be attributed to the lack of theory explaining an overall profile of signal. The previous chapter showed how one could utilize the symmetric and anti-symmetric integrated response functions [34] to characterize the role of stability matrix in 1D plots. These functions cannot separate the contribution of nonlinear polarizability from that of anharmonicity of potentials, but can isolate the contribution of the stability matrix from that of the simple three-point correlation function. The role of stability matrix is important in terms of equilibrium simulation, whereas the comparison of the term of nonlinear polarizability with that of anharmonicity is essential with respect to the normal mode (NM) analysis.

This chapter presents a practical method to evaluate the relative contributions of nonlinear polarizability and anharmonicity of potentials from the experimental and simulation data. These contributions can be estimated from analytical theories [3] or MD simulations [6][13] by turning on and off the terms responsible for the contributions; however, it has not been possible to analyze directly the experimental data especially for multi-mode systems due to the complication of the 2D maps. Our approach can extract quantitative information about the ratio between the nonlinear polarizability and anharmonicity of potentials in the molecular system. To evaluate this ratio, we have derived the analytical expression of the fifth-order Raman signal for an anharmonic potential system based on a perturbative calculation of a Morse oscillator system.[3] [13] By carrying out the double Fourier transformation of the 2D time domain Raman signal, we have obtained the frequency domain expressions of the fifth-order Raman signal. The analysis of spectral volumes gives access to the ratio between nonlinear polarizability and anharmonicity, which reveals the change of molecular mechanisms between solid and liquid phases. [7]

In Sec.3-2, we have derived the expression of fifth-order response functions in the frequency domain. The derivation of the analytical expression for anharmonicity term is explained in Appendix. In Sec.3-3, we have applied our method to simple liquids described by a Lennard-Jones (LJ) potential and showed that we can clarify each vibrational mode uniquely by using 2D frequency domain maps. The NM expressions using the calculated ratio between nonlinear polarizability and anharmonicity are compared with MD simulation results.[13] In Sec.3-4, we have further applied our method to the soft core potential systems to investigate a role of nonlinear polarizability and anharmonicity, which was not clarified in our previous study.[7] Section 3-5 is devoted to the concluding remarks.

3-2. Frequency-domain Signals of Fifth-order Raman Spectroscopy

The fifth-order Raman response function is defined by a three-body correlation function of polarizability. In this section, we demonstrate how one can obtain the information of the nonlinear polarizability and anharmonicity from the experimental and simulation data by using the analytical expression of the response function.

We assume the polarizability with ab tensor, $\Pi_{ab}(t)$, is expanded in terms of a single molecular coordinate $q(t)$ as

$$\Pi_{ab}(t)-\Pi_{ab}=\Pi'_{ab}q(t)+\frac{\lambda}{2}\Pi''_{ab}q(t)^2+\cdots, \tag{3.1}$$

where λ is a perturbation index which is set to unity after completion of the perturbation expansion. The molecular coordinate is treated as a harmonic motion $q_H(t)$ plus a perturbative anharmonic motion $q_A(t)$,

$$q(t)=q_H(t)+\lambda q_A(t). \tag{3.2}$$

The fifth-order response function $R^{(5)}_{abcdef}(t_2,t_1)$ is expressed as

$$R^{(5)}_{abcdef}(t_2,t_1)=R^{(5)}_{abcdef,LT}(t_2,t_1)+\lambda\left(R^{(5)}_{abcdef,NL}(t_2,t_1)+R^{(5)}_{abcdef,AN}(t_2,t_1)\right), \tag{3.3}$$

where

$$R^{(5)}_{abcdef,LT}(t_2,t_1)=\frac{1}{kT}\left\langle\Pi'_{ab}\Pi'_{cd}\Pi'_{ef}M_H(t_2,0)\dot{q}_H(-t_1)\right\rangle \tag{3.4}$$

and

$$\begin{aligned}R^{(5)}_{abcdef,NL}(t_2,t_1)=&\frac{1}{kT}\left\langle\Pi''_{ab}\Pi'_{cd}\Pi'_{ef}M_H(t_2,0)q_H(t_2)\dot{q}_H(-t_1)\right\rangle\\&+\frac{1}{kT}\left\langle\Pi'_{ab}\Pi''_{cd}\Pi'_{ef}M_H(t_2,0)q_H(0)\dot{q}_H(-t_1)\right\rangle\\&+\frac{1}{kT}\left\langle\Pi'_{ab}\Pi'_{cd}\Pi''_{ef}M_H(t_2,0)q_H(-t_1)\dot{q}_H(-t_1)\right\rangle\end{aligned} \tag{3.1}$$

are the contributions from linear and nonlinear polarizability, and

$$R^{(5)}_{abcdef,AN}(t_2,t_1)=\frac{1}{kT}\left\langle\Pi'_{ab}\Pi'_{cd}\Pi'_{ef}M_A(t_2,0)\dot{q}_H(-t_1)\right\rangle+\frac{1}{kT}\left\langle\Pi'_{ab}\Pi'_{cd}\Pi'_{ef}M_H(t_2,0)\dot{q}_A(-t_1)\right\rangle \tag{3.6}$$

is that from anharmonicity of potentials. Here, $M(t_2,t_1)=M_H(t_2,t_1)+\lambda M_A(t_2,t_1)$ is the stability matrix for harmonic and anharmonic parts of trajectories, and kT represents the temperature multiplied by Boltzmann constant.

In the Brownian oscillator (BO) model, the linear polarizability term vanishes and the nonlinear polarizability term is reduced to [2] [3] [4]

$$\begin{aligned}R^{(5)}_{abcdef,NL}(t_2,t_1)\propto&\left\langle\Pi'_{ab}\Pi''_{cd}\Pi'_{ef}\right\rangle\int d\omega\frac{\rho(\omega)}{\omega^2}C''(t_2)C''(t_1)\\&+\left\langle\Pi''_{ab}\Pi'_{cd}\Pi'_{ef}\right\rangle\int d\omega\frac{\rho(\omega)}{\omega^2}C''(t_2)C''(t_1+t_2)\end{aligned}, \tag{3.7}$$

where $C''(t)=\sin(\omega t)e^{-\gamma t}$ and the decay rate, γ, is assumed to be independent of ω in order to simplify the following discussion. Hereafter, we adopt the BO model with an exponential decay and do not take a bi-exponential decay. The expressions of decay functions do not make much difference on the following procedure and discussion about the ratio between nonlinear polarizability and anharmonicity of potentials.

Since the fifth-order signal calculated from the BO approach does not involve the anharmonic contribution, it disagrees with the direct evaluation of the response function by means of MD simulations. In order to improve the BO approach and evaluate $R^{(5)}_{abcdef,AN}(t_2,t_1)$, we analytically calculate $q_H(t)$ and $q_A(t)$ for a Morse potential,

$$V(q)=D\left(e^{-2\beta q}-2e^{-\beta q}\right), \tag{3.8}$$

from the perturbative expansion approach, where β and D are potential parameters. We then derived the anharmonicity part of the fifth-order response function as

$$R^{(5)}_{abcdef,AN}(t_2,t_1)\propto\beta\left\langle\Pi'_{ab}\Pi'_{cd}\Pi'_{ef}\right\rangle\int d\omega\frac{\rho(\omega)}{\omega^2}4C''^3\left(\frac{t_2}{2}\right)C''\left(t_1+\frac{t_2}{2}\right). \tag{3.9}$$

An explicit derivation of Eq. (3.9) is given in Appendix, where we compare Eq. (3.9) with the anharmonic part of the fifth-order response function for the anharmonicity additive potential and show the accordance of Eq. (3.9) with the expressions obtained by Okumura and Tanimura and by Ma and Stratt when $g_3=-6D\beta^3$.[3] [13]

The anharmonic term (3.9), together with the nonlinear term (3.7), casts the total fifth-order response function into the form,

$$\begin{aligned}R^{(5)}_{abcdef}(t_2,t_1)\propto&\left\langle\Pi'_{ab}\Pi''_{cd}\Pi'_{ef}\right\rangle\int d\omega\frac{\rho(\omega)}{\omega^2}C''(t_2)C''(t_1)\\&+\left\langle\Pi''_{ab}\Pi'_{cd}\Pi'_{ef}\right\rangle\int d\omega\frac{\rho(\omega)}{\omega^2}C''(t_2)C''(t_1+t_2)\\&-\beta\left\langle\Pi'_{ab}\Pi'_{cd}\Pi'_{ef}\right\rangle\int d\omega\frac{\rho(\omega)}{\omega^2}4C''^3\left(\frac{t_2}{2}\right)C''\left(t_1+\frac{t_2}{2}\right)\end{aligned}. \tag{3.10}$$

If $a=c$ and $b=d$, we can recast Eq. (3.10) as

$$\begin{aligned}R^{(5)}_{abcdef}(t_2,t_1)\propto\int d\omega\frac{\rho(\omega)}{\omega^2}\Big\{&k_{abcdef,NL}(\omega)C''(t_2)\left(C''(t_1)+C''(t_1+t_2)\right)\\&+k_{abcdef,AN}(\omega)\cdot4C''^3\left(\frac{t_2}{2}\right)C''\left(t_1+\frac{t_2}{2}\right)\Big\}\end{aligned}, \tag{3.11}$$

where the intensities of the nonlinear polarizability and anharmonicity are now denoted by $k_{abcdef,NL}(\omega)$ and $k_{abcdef,AN}(\omega)$, respectively. As is illustrated below, $k_{abcdef,NL}(\omega)$ and $k_{abcdef,AN}(\omega)$ can be evaluated quantitatively from the experimental and simulation data with use of the double Fourier transformation of the response function defined by

$$\begin{aligned}\tilde{R}^{(5)}_{abcdef}(\omega_2,\omega_1) &= \int_0^\infty dt_1 \sin(\omega_1 t_1)\int_0^\infty dt_2 \sin(\omega_2 t_2) R^{(5)}_{abcdef}(t_2,t_1) \\ &= \mathrm{Im}\left\{\int_0^\infty dt_1 e^{i\omega_1 t_1}\,\mathrm{Im}\left\{\int_0^\infty dt_2 e^{i\omega_2 t_2} R^{(5)}_{abcdef}(t_2,t_1)\right\}\right\}\end{aligned}. \tag{3.12}$$

The substitution of Eq. (3.11) into Eq. (3.12) leads to the expression without tensor elements as

$$\begin{aligned}\tilde{R}^{(5)}(\omega_2,\omega_1) \propto \int d\omega \frac{\rho(\omega)}{\omega^2}\Big\{ & k_{NL}(\omega)\left(\tilde{R}_{0,NL}(\omega_2,\omega_1;\omega)+\tilde{R}_{1,NL}(\omega_2,\omega_1;\omega)+\tilde{R}_{2,NL}(\omega_2,\omega_1;\omega)\right) \\ & + k_{AN}(\omega)\left(\tilde{R}_{0,AN}(\omega_2,\omega_1;\omega)+\tilde{R}_{1,AN}(\omega_2,\omega_1;\omega)+\tilde{R}_{2,AN}(\omega_2,\omega_1;\omega)\right)\Big\}\end{aligned}, \tag{3.13}$$

where

$$\tilde{R}_{0,NL}(\omega_2,\omega_1;\omega) = \frac{1}{2}\cdot\frac{(\omega_1-\omega)\omega_2}{\left((\omega_1-\omega)^2+\gamma^2\right)\left(\omega_2{}^2+4\gamma^2\right)}, \tag{3.14}$$

$$\tilde{R}_{1,NL}(\omega_2,\omega_1;\omega) = \frac{\gamma^2}{\left((\omega_1-\omega)^2+\gamma^2\right)\left((\omega_2-\omega)^2+\gamma^2\right)}, \tag{3.15}$$

$$\tilde{R}_{2,NL}(\omega_2,\omega_1;\omega) = \frac{1}{2}\cdot\frac{2\gamma^2-(\omega_1-\omega)(\omega_2-2\omega)}{\left((\omega_1-\omega)^2+\gamma^2\right)\left((\omega_2-2\omega)^2+4\gamma^2\right)}, \tag{3.16}$$

$$\tilde{R}_{0,AN}(\omega_2,\omega_1;\omega) = \frac{3}{2}\cdot\frac{(\omega_1-\omega)\omega_2}{\left((\omega_1-\omega)^2+\gamma^2\right)\left(\omega_2{}^2+4\gamma^2\right)}. \tag{3.17}$$

$$\tilde{R}_{1,AN}(\omega_2,\omega_1;\omega) = \frac{\gamma^2-2(\omega_1-\omega)(\omega_2-\omega)}{\left((\omega_1-\omega)^2+\gamma^2\right)\left((\omega_2-\omega)^2+\gamma^2\right)}, \tag{3.18}$$

and

$$\tilde{R}_{2,AN}(\omega_2,\omega_1;\omega) = \frac{1}{2}\cdot\frac{-2\gamma^2+(\omega_1-\omega)(\omega_2-2\omega)}{\left((\omega_1-\omega)^2+\gamma^2\right)\left((\omega_2-2\omega)^2+4\gamma^2\right)}. \tag{3.19}$$

If we set $\rho(\omega)=\delta(\omega-\omega_a)$, the signal consists of two peaks centered at $\omega_1=\omega_2=\omega_a$ and $\omega_1=\omega_2/2=\omega_a$ as

$$\tilde{R}^{(5)}_{obs}(\omega_2,\omega_1) \propto k_{NL}(\omega_a)\frac{1}{(\omega_1-\omega_a)^2+\gamma^2}\left(\frac{1}{(\omega_2-\omega_a)^2+\gamma^2}+\frac{1}{2}\cdot\frac{2}{(\omega_2-2\omega_a)^2+4\gamma^2}\right) + k_{AN}(\omega_a)\frac{1}{(\omega_1-\omega_a)^2+\gamma^2}\left(\frac{1}{(\omega_2-\omega_a)^2+\gamma^2}-\frac{1}{2}\cdot\frac{2}{(\omega_2-2\omega_a)^2+4\gamma^2}\right). \quad (3.20)$$

In a real system the spectral distribution $\rho(\omega)$ may not be a delta-function, and the terms such as

$$\int d\omega \frac{\rho(\omega)}{\omega^2}\frac{(\omega_1-\omega)(\omega_2-\omega)}{((\omega_1-\omega)^2+\gamma^2)((\omega_2-\omega)^2+\gamma^2)} \quad (3.21)$$

can also make a contribution to the spectra. Therefore the profiles and positions of peaks are slightly displaced from those predicted by Eq. (3.20). In the case that $\rho(\omega)$ has a Gaussian like profile, however, the contributions of Eq. (3.21) to the spectral volume centered at $\omega \approx \omega_a$ is negligible because we have

$$\int_{\omega_a-\Delta\omega}^{\omega_a+\Delta\omega} d\omega_2 \int_{\omega_a-\Delta\omega}^{\omega_a+\Delta\omega} d\omega_1 \int d\omega \frac{\rho(\omega)}{\omega^2}\frac{(\omega_1-\omega)(\omega_2-\omega)}{((\omega_1-\omega)^2+\gamma^2)((\omega_2-\omega)^2+\gamma^2)} \approx 0, \quad (3.22)$$

where $\Delta\omega$ represents the spectral width. If a frequency-resolved spectrum obtained from either the experiments or simulations is expressed as

$$\tilde{R}^{(5)}_{obs}(\omega_2,\omega_1) = \tilde{R}^{(5)}_{obs}(\omega_2 \approx \omega_a, \omega_1 \approx \omega_a) + \tilde{R}^{(5)}_{obs}(\omega_2 \approx 2\omega_a, \omega_1 \approx \omega_a), \quad (3.23)$$

the contributions from the nonlinear polarizability and anharmonicity for each molecular motion can be evaluated through the following equation,

$$\frac{k_{AN}(\omega_a)}{k_{NL}(\omega_a)} \approx \frac{\tilde{R}^{(5)}_{obs}(\omega_a,\omega_a) - 2\tilde{R}^{(5)}_{obs}(2\omega_a,\omega_a)}{\tilde{R}^{(5)}_{obs}(\omega_a,\omega_a) + 2\tilde{R}^{(5)}_{obs}(2\omega_a,\omega_a)}. \quad (3.24)$$

We now consider the method to separate the peak near $\omega_1 = \omega_2 = \omega_a$ from other peaks, for example, near $\omega_1 = \omega_2/2 = \omega_a$. If $\tilde{R}^{(5)}_{obs}(\omega_2,\omega_1) - \tilde{R}^{(5)}_{obs}(\omega_1,\omega_2)$ is calculated, Eqs. (3.15) and (3.18) vanish because of the symmetry with respect to ω_1 and ω_2 for any $\rho(\omega)$. Moreover, by using $\tilde{R}^{(5)}_{obs}(\omega_2,\omega_1) - \tilde{R}^{(5)}_{obs}(\omega_1,\omega_2)$, we can remove the cross peaks which often overlap with the peak at $\omega_1 = \omega_2/2$ in a multimode system. The volume of each peak can be measured accurately as illustrated in Secs. 3-3 and 3-4. Hereafter, we discuss *abcd* = *zzzz* and *abcdef* = *zzzzzz* tensors in the response functions, and drop the suffixes for simplicity.

3-3. Analyzing the Two-dimensional Signals of Lennard-Jones Systems

Using 2D frequency domain maps, we can also clarify the peaks more clearly than 1D frequency domain plots. In this section, we apply our method to the fifth-order 2D Raman signals of the LJ potential system, which were well investigated by Ma and Stratt, [12][13] to evaluate the consistency of the ratio k_{AN}/k_{NL}. At the same time, we demonstrate a way to judge whether the spectral peak is composed of a single mode or multi-modes.

We calculate the fifth-order Raman signals in the LJ potential system by the equilibrium and non-equilibrium hybrid method.[11] Then, we transformed the signals from time domain to frequency domain with a Welch window function. MD simulations are carried out with 108 LJ atoms. The same potential, polarizability, size of the simulation box, and time step used in these simulations are used as those of Ma and Stratt's simulation.[12] [13] The forces by LJ potential and DID interaction are smoothly cut off at the half length of the simulation box with the switching function. In the non-equilibrium calculations, the system is irradiated by laser pulse pairs with the strength of 5.0 V/A. The third- and fifth-order response functions are calculated by averaging over 4,000,000 configurations.

The 1D frequency domain plot of the third-order response function, $\tilde{R}^{(3)}(\omega)$, is shown in Fig. 3.1. We found that the signal may be fit by either one Lorentzian peak or three Gaussian peaks, which are depicted in Fig. 3.1(a) and (b), respectively.[30] Figures 3.2(a) and (b) show the 2D contour plots in frequency domain, $\tilde{R}^{(5)}(\omega_2,\omega_1)$ and $\tilde{R}^{(5)}(\omega_2,\omega_1)-\tilde{R}^{(5)}(\omega_1,\omega_2)$, respectively. These figures indicate that the dynamics in the LJ potential system is governed by one mode. Thus, $\tilde{R}^{(3)}(\omega)$ should be fit with a single Gaussian peak as Fig. 3.1(b), and the frequency for the translational motion is found to be about $19\,\mathrm{cm}^{-1}$.

As shown in Fig. 3.2(b), $\tilde{R}^{(5)}(\omega_2,\omega_1)-\tilde{R}^{(5)}(\omega_1,\omega_2)$ allows us to specify the peak near $\omega_1=\omega_2/2=19\,\mathrm{cm}^{-1}$ more easily than $\tilde{R}^{(5)}(\omega_2,\omega_1)$ does. The calculated ratio of the spectral volumes, $\tilde{R}^{(5)}(\omega_1=\omega_2/2)/\tilde{R}^{(5)}(\omega_1=\omega_2)$, is -0.30, which gives us $k_{AN}/k_{NL}=4.0$ for the translational mode. In fact, if we adapt this ratio and calculate the diagonal element on $t_1=t_2$ and t_2 axis element on $t_1=0$ of Eq. (3.10) according to the NM expressions using the third-order response function $R^{(3)}(t)$ as

$$R^{(5)}(t,t) \propto k_{NL}\int_0^t dt\left(\frac{3}{2}R^{(3)}(3t)+R^{(3)}(2t)-\frac{1}{2}R^{(3)}(t)\right) + k_{AN}\int_0^t dt\left(-3R^{(3)}(3t)+6R^{(3)}(2t)-3R^{(3)}(t)\right) \tag{3.25}$$

and

$$R^{(3)}(t,0) \propto k_{NL}\int_0^t dtR^{(3)}(2t)+k_{AN}\int_0^t dt\left(-R^{(3)}(2t)+2R^{(3)}(t)\right), \tag{3.26}$$

we can well reconstruct the original fifth-order response function in the short time region as plotted in Fig. 3.2(c). The large deviations of Eqs. (3.25) and (3.26) from MD simulations over 200 fs are attributed to the use of the NM expression instead of BO expression. Moreover, the agreement of these results with Fig. 7 in Ref. [13] strongly supports the ability to evaluate the ratio between anharmonicity and nonlinearity from the present our method.

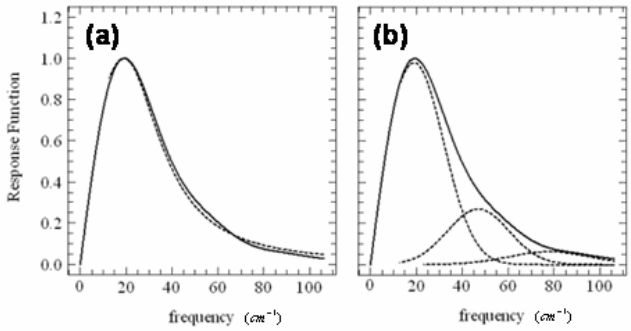

Figure 3.1. The third-order response functions $\tilde{R}^{(3)}(\omega)$ are depicted as the solid line. (a) The curve fitted with one Lorenzian peak and (b) the curves fitted with three Gaussian peaks are plotted as the dashed lines.

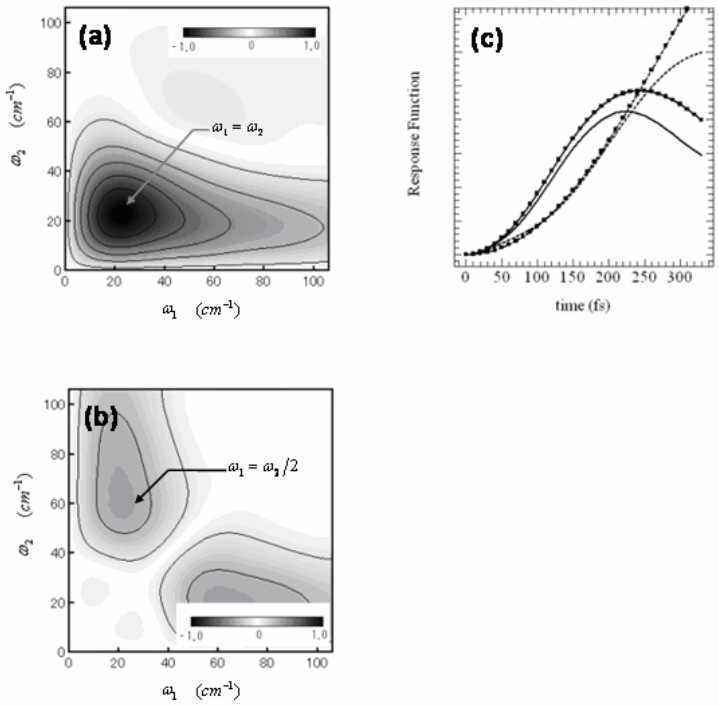

Figure 3.2. (a) The fifth-order response function $\tilde{R}^{(5)}(\omega_2,\omega_1)$, and (b) $\tilde{R}^{(5)}(\omega_2,\omega_1)-\tilde{R}^{(5)}(\omega_1,\omega_2)$ for the LJ system at $T=220\,\mathrm{K}$ are depicted. In Fig. (c), The MD results along $t_1=t_2$ (solid line) and $t_1=0$ (dotted line) are compared with the signals calculated from Eqs. (3.25) (solid line with circle markers) and (26) (dotted line with circle markers), respectively.

The temperature dependence of the ratio k_{NL}/k_{AN} is investigated at $T=95$, 120, and 160 K for the supercooled liquids and at $T=220$ and 260 K for the normal liquids under same density, and is shown in Fig. 3.3.[35] In Fig. 3.3, this ratio seems almost constant in both phases, which means that fifth-order response function cannot capture the qualitative change between both liquids. Although the mobility is changed in general between both liquids, its effect does not appear in short time scale of the present simulation.

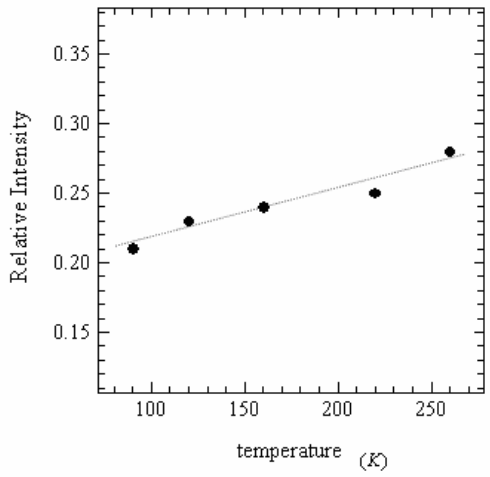

Figure 3.3. The ratio of k_{NL}/k_{AN} for the LJ potential system is illustrated as the function of temperature. The dashed line is a guide for eyes.

3-4. Analyzing the Two-dimensional Signals of Soft Core Systems

We investigate the soft-core potential system defined by the potential,

$$U(r)=\varepsilon\left(\frac{\sigma}{r}\right)^{6}+A\left(\frac{r}{\sigma}\right)^{4}+B, \tag{3.27}$$

where ε and σ are the potential parameters, and the constants A and B are chosen to connect the force and potential smoothly at the cutoff r_0. Thus A and B are given by $3/2\,\varepsilon(\sigma/r_0)^{10}$ and $-5/2\cdot\varepsilon(\sigma/r_0)^{6}$, respectively. We carried out the MD simulation in reduced units. A temperature multiplied by Boltzmann constant is changed from solid phase ($kT=0.14,0.155$) to liquid phase ($kT=0.20,0.215,0.23$) as a parameter with fixed density. The other conditions on the simulation are the same as the previously study[7] in which we found that the fifth-order Raman signals are sensitive to the difference of the phases, while the third-order Raman signals are not. The method developed in this study sheds light on the relative intensities of the nonlinear polarizability and anharmonicity on the fifth-order signals.

The 1D time domain and frequency domain plots, $R^{(3)}(t)$ and $\tilde{R}^{(3)}(\omega)$, 2D time domain and frequency domain maps, $R^{(5)}(t_2,t_1)$ and $\tilde{R}^{(5)}(\omega_2,\omega_1)$, and $\tilde{R}^{(5)}(\omega_2,\omega_1)-\tilde{R}^{(5)}(\omega_1,\omega_2)$ at $kT=0.14$ are depicted in Figs. 3.4(a), (b), (c), (d), and (e), respectively, and at $kT=0.20$ are shown in Fig. 3.5(a), (b), (c), (d), and (e), respectively. Figure 3.4(b) exhibits a

similar profile to Fig. 3.5(b) and the 1D frequency domain maps in the other temperatures. These signals are also similar to the LJ case depicted in Fig. 3.1. On the other hand, we can clearly see the difference of 2D signals in the soft-core and LJ cases; the 2D signals of soft-core potential system consist of two modes. The frequency of two modes are found to be $\omega_l = 6.5$ and $\omega_h = 16$, respectively. The modes of ω_l and ω_h are thought to be from delocalized vibrational motion for each atom and high frequency localized mode, respectively.[36]

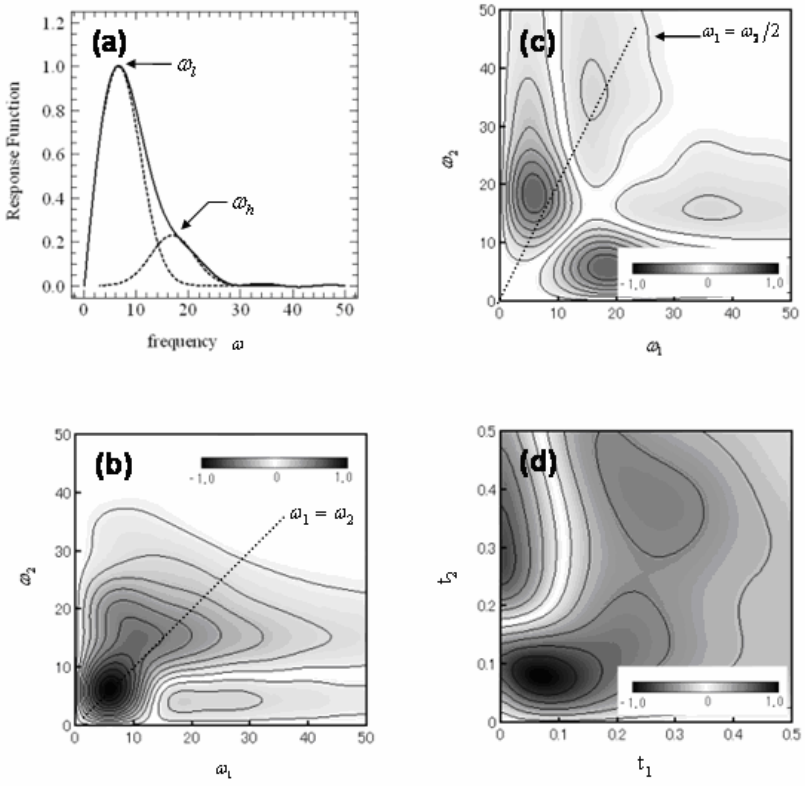

Figure 3.4. (a) The third-order response function $\tilde{R}^{(3)}(\omega)$ and the fifth-order response functions, (b) $\tilde{R}^{(5)}(\omega_2,\omega_1)$ and (c) $\tilde{R}^{(5)}(\omega_2,\omega_1)-\tilde{R}^{(5)}(\omega_1,\omega_2)$, for the soft core system at $kT = 0.140$ are depicted. (d) The time domain 2D maps $R^{(5)}(t_2,t_1)$ are shown for comparison (see reference 9). The curve fitted to the third-order spectrum with two Gaussian peaks is presented as the dotted line. All figures are in reduced units.

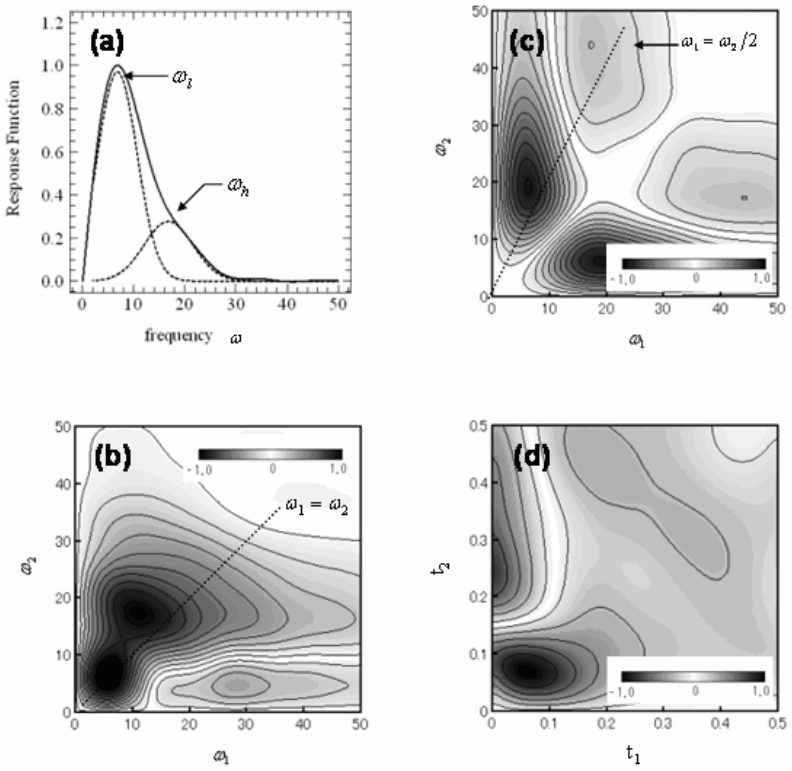

Figure 3.5. (a) The third-order response function $\tilde{R}^{(3)}(\omega)$ and the fifth-order response functions, (b) $\tilde{R}^{(5)}(\omega_2,\omega_1)$ and (c) $\tilde{R}^{(5)}(\omega_2,\omega_1)-\tilde{R}^{(5)}(\omega_1,\omega_2)$, for the soft core system at $kT=0.200$ are depicted. (d) The time domain 2D maps $R^{(5)}(t_2,t_1)$ are shown for comparison (see reference 9). The curve fitted to the third-order spectrum with two Gaussian peaks is presented as the dotted line. All figures are in reduced units.

The relative intensities of the nonlinear polarizability and anharmonicity for ω_l and ω_h are determined from the spectral volumes of 2D frequency domain maps as summarized in Table 1. The calculated ratios for each mode are visualized in Fig. 3.6 for $k_{NL}(\omega_l)/k_{AN}(\omega_l)$, $k_{AN}(\omega_h)/k_{AN}(\omega_l)$, and $k_{AN}(\omega_h)/k_{AN}(\omega_h)$. All ratios except for the nonlinear polarizability at ω_l show almost proportional to each other at any temperature, while the ratios between $k_{NL}(\omega_l)$ and the other intensities exhibit a specific phase dependency as shown in Fig. 3.6. Thus, we may consider that the nonlinear polarizability of the delocalized mode is dramatically changed, whereas the high frequency localized mode is not changed as long as

the fifth-order Raman spectra can capture. This consideration indicates that the difference of the anti-symmetric integrated response functions between solid and liquid phases [7] is induced by the nonlinear polarizability of ω_l. In addition, the anharmonicity makes larger contribution to the fifth-order signal than the nonlinear polarizability for the localized mode, while makes smaller contribution for delocalized mode as shown in Table 1.

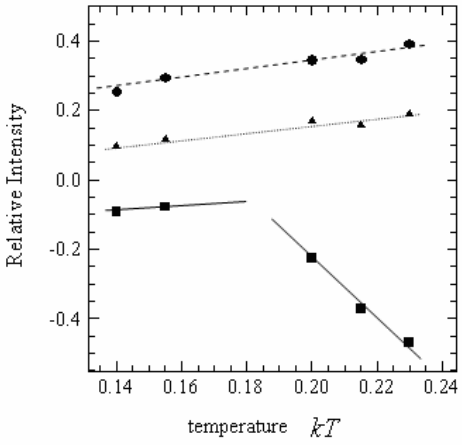

Figure 3.6. The ratios of $k_{NL}(\omega_l)/k_{AN}(\omega_l)$ (square), $k_{AN}(\omega_h)/k_{AN}(\omega_l)$ (triangle), and $k_{AN}(\omega_h)/k_{NL}(\omega_h)$ (circle) for the soft-core potential system are illustrated as the function of temperature. All lines are guides for eyes.

Table 1; Relative ratios between anharmonicity of potentials and nonlinearlity of polarizability

temperature	ω_l		ω_h	
kT	AN	NL	AN	NL
0.140	2.6	-0.24	0.25	1.0
0.155	2.5	-0.21	0.25	1.0
0.200	2.0	-0.46	0.34	1.0
0.215	2.2	-0.82	0.35	1.0
0.230	2.1	-0.97	0.39	1.0

3-5. Conclusion

In this section, we proposed the method to evaluate the contributions from the nonlinear polarizability and anharmonicity of potentials utilizing the analytical expression of 2D signals in frequency domain. The ratio between two contributions was evaluated from the volumes of spectral peaks. With 2D Raman frequency domain maps, we could easily separate contributions from different vibrational modes, which was difficult with 1D approach.

Demonstration to apply our method to the simulation results for LJ potential system indicates that primary contribution of molecular motions to the signal comes from only a translational mode at 19 cm^{-1}. Moreover we evaluated the ratio between nonlinear polarizability and anharmonicity as $k_{AN}/k_{NL} = 4.0$. Good agreement is obtained in comparison of the NM expression of the fifth-order response functions using this ratio with the data of Ma and Stratt,[13] which supports the consistency of our method.

We also examined our method to analyze the signals of the soft-core potential system at various temperatures. In our previous study,[7] it was found that the 2D time domain Raman signals exhibited a clear difference between the solid and liquid phases, but the origin of this difference could not be identified. The present method shows that the different fifth-order Raman signals between both phases resulted from the change of the mode of ω_l through the nonlinear polarizability. At the same time, the phase transition was shown to have little effect on the mode of ω_h . We can conclude from the fifth-order response function that the dynamical change between the solid and liquid phases is characterized as not high frequency localized mode but delocalized motion in soft core potential systems. Moreover when our attention is paid to the contributions to the fifth-order signal, we can find that the nonlinear polarizability and anharmonicity of potential are dominant for the localized and delocalized modes, respectively.

3-6. Appendix: Derivation of the Anharmonic Contribution in Morse Potential System

The contribution of anharmonicity to the fifth-order Raman signal was first evaluated by Okumura and Tanimura using Feynman rules for anharmonicity additive potential.[3] Then,

by using the adiabatic instantaneous normal mode theory, Ma and Stratt derived the same expression as Okumura and Tanimura.[13] Here, we show the same expression can be obtained from the perturbative calculations by assuming a Morse potential system defined by Eq. (3.8). When the correspondence of the anharmonicity additive potential

$$V(q)=\frac{\mu\omega^2}{2}q^2(t)+\frac{g_3}{3!}q^3(t) \tag{3.28}$$

with the Morse potential is taken into consideration, we can obtain the relations, $\omega=\beta\sqrt{2D/\mu}$ and $g_3=-6D\beta^3$, by expanding the Morse potential with respect of q. We may evaluate the fifth-order response function from the solution of the Morse potential, because the contributions of the nonlinear polarizability and anharmonicity over λ^2 are negligible at small q.

The equation of motion for the Morse potential system can be solved analytically and the coordinate and momentum are given by

$$q(t)=\frac{1}{\beta}\ln\frac{1+\sqrt{1-C_1}\sin\left(\sqrt{\frac{2DC_1}{\mu}}\beta t+C_2\right)}{C_1}, \tag{3.29}$$

and

$$p(t)=\sqrt{2\mu DC_1}\frac{\sqrt{1-C_1}\cos\left(\sqrt{\frac{2DC_1}{\mu}}\beta t+C_2\right)}{1+\sqrt{1-C_1}\sin\left(\sqrt{\frac{2DC_1}{\mu}}\beta t+C_2\right)}, \tag{3.30}$$

where μ is the mass of molecule, and C_1 and C_2 are the integral constants. When we expand Tayler series up to the first-order around the bottom of the Morse potential, the position and momentum are written as

$$q(t)=\frac{1}{\beta}\left(\sqrt{1-C_1}\sin\left(\sqrt{\frac{2D}{\mu}}\beta t+C_2\right)-\frac{1-C_1}{2}\left(-2+\sin^2\left(\sqrt{\frac{2D}{\mu}}\beta t+C_2\right)\right)+\cdots\right) \tag{3.31}$$

and

$$p(t)=\sqrt{2D\mu}\left(\sqrt{1-C_1}\cos\left(\sqrt{\frac{2D}{\mu}}\beta t+C_2\right)-\frac{1-C_1}{2}\sin\left(2\left(\sqrt{\frac{2D}{\mu}}\beta t+C_2\right)\right)+\cdots\right). \tag{3.32}$$

Using these solutions, we can calculate the stability matrix analytically as

$$\frac{\partial q(t)}{\partial p(0)} = \frac{1}{\beta\sqrt{2D\mu}}\left(\sin\left(\sqrt{\frac{2D}{\mu}}\beta t\right) + 4\sqrt{1-C_1}\sin\left(\sqrt{\frac{D}{2\mu}}\beta t + C_2\right)\sin^3\left(\sqrt{\frac{D}{2\mu}}\beta t\right) + \cdots\right). \tag{3.33}$$

Thus

$$q_H(t) = \frac{\sqrt{1-C_1}}{\beta}\sin\left(\sqrt{\frac{2D}{\mu}}\beta t + C_2\right), \tag{3.34}$$

$$q_A(t) = -\frac{1-C_1}{2\beta}\left(-2 + \sin^2\left(\sqrt{\frac{2D}{\mu}}\beta t + C_2\right)\right), \tag{3.35}$$

$$M_H(t) = \frac{1}{\beta\sqrt{2D\mu}}\sin\left(\sqrt{\frac{2D}{\mu}}\beta t\right), \tag{3.36}$$

and

$$M_A(t) = \frac{4\sqrt{1-C_1}}{\beta\sqrt{2D\mu}}\sin\left(\sqrt{\frac{D}{2\mu}}\beta t + C_2\right)\sin^3\left(\sqrt{\frac{D}{2\mu}}\beta t\right). \tag{3.37}$$

The substitutions of these equations into Eqs. (3.3), (3.4), (3.5), and (3.6) give us the expression for the anharmonicity of potentials as

$$\begin{aligned} R^{(5)}_{abcdef}(t_2,t_1) = {} & \frac{1}{kT}\left\langle \Pi''_{ab}\Pi'_{cd}\Pi'_{ef}\,\frac{(1-C_1)}{\mu\beta^2}\sin\left(\sqrt{\frac{2D}{\mu}}\beta t_2\right)\sin\left(\sqrt{\frac{2D}{\mu}}\beta(t_1+t_2)\right)\right\rangle \\ & + \frac{1}{kT}\left\langle \Pi'_{ab}\Pi''_{cd}\Pi'_{ef}\,\frac{(1-C_1)}{\mu\beta^2}\sin\left(\sqrt{\frac{2D}{\mu}}\beta t_2\right)\sin\left(\sqrt{\frac{2D}{\mu}}\beta t_1\right)\right\rangle \\ & + \frac{1}{kT}\left\langle \Pi'_{ab}\Pi'_{cd}\Pi'_{ef}\,\frac{4(1-C_1)}{\mu\beta}\sin^3\left(\sqrt{\frac{D}{2\mu}}\beta t_2\right)\sin\left(\sqrt{\frac{2D}{\mu}}\beta t_1 + \sqrt{\frac{D}{2\mu}}\beta t_2\right)\right\rangle \end{aligned} . \tag{3.38}$$

When the relations $\omega = \beta\sqrt{2D/\mu}$ and $(1-C_1)/D = \mu\omega^2 q^2/2 = kT/2$ are used, Eq. (3.38) becomes

$$\begin{aligned} R^{(5)}_{abcdef}(t_2,t_1) \propto {} & \left\langle \Pi''_{ab}\Pi'_{cd}\Pi'_{ef}\,\frac{1}{\omega^2}\sin(\omega t_2)\sin(\omega t_1+\omega t_2)\right\rangle \\ & + \left\langle \Pi'_{ab}\Pi''_{cd}\Pi'_{ef}\,\frac{1}{\omega^2}\sin(\omega t_2)\sin(\omega t_1)\right\rangle \\ & - \left\langle \Pi'_{ab}\Pi'_{cd}\Pi'_{ef}\,\frac{4\beta}{\omega^2}\sin^3(\omega t_2)\sin\left(\omega t_1 + \frac{\omega}{2}t_2\right)\right\rangle \end{aligned} . \tag{3.39}$$

The expression for the anharmonicity additive potential is obtained by setting $g_3 = -6D\beta^3$, which has the same form as the expressions obtained by Okumura and Tanimura and by Ma and Stratt.

3-7. Reference

[1] S. Mukamel, *Principles of Nonlinear Optical Spectroscopy* (Oxford University Press, 1995).

[2] Y. Tanimura and S. Mukamel, J. Chem. Phys. **99**, 9496 (1993).

[3] K. Okumura and Y. Tanimura, J. Chem. Phys. **107**, 2267 (1997).

[4] S. Saito and I. Ohmine, J. Chem. Phys. **108**, 240 (1998).

[5] S. Saito and I. Ohmine, Phys. Rev. Lett. **88**, 207401 (2002).

[6] S. Saito and I. Ohmine, J. Chem. Phys. **119**, 9073 (2003).

[7] Y. Nagata and Y. Tanimura, J. Chem. Phys. **124**, 024508 (2006).

[8] T. l. C. Jansen, J.G. Snijders, and K. Duppen, J. Chem. Phys. **113**, 307 (2000)

[9] T. l. C. Jansen, J. G. Snijders, and K. Duppen, *ibid*. **114,** 10910 (2001).

[10] T. l. C. Jansen, K. Duppen, and J. G. Snijders, Phys. Rev. B **67**, 134206 (2003).

[11] T. Hasegawa and Y. Tanimura, J. Chem. Phys. **125**, 074512 (2006).

[12] A. Ma and R. M. Stratt, Phys. Rev. Lett. **85**, 1004 (2000).

[13] A. Ma and R. M. Stratt, J. Chem. Phys. **116**, 4972 (2002).

[14] R. DeVane, C. Ridley, B. Space, and T. Keyes, J. Chem. Phys. **119**, 6073 (2003).

[15] R. L. Murry, J. T. Fourkas, and T. Keyes, J. Chem. Phys. **109**, 7913 (1998).

[16] J. Kim and T. Keyes, Phys. Rev. E **65**, 061102 (2002).

[17] T. Keyes and J. T. Fourkas, J. Chem. Phys. **112**, 287 (2000).

[18] A. Piryatinski, C. P. Lawrence, and J. L. Skinner, J. Chem. Phys. **118**, 9664 (2003).

[19] A. Piryatinski, C. P. Lawrence, and J. L. Skinner, J. Chem. Phys., **118**, 9672 (2003).

[20] R. Akiyama and R. F. Loring, J. Chem. Phys. **116**, 4655 (2002).

[21] S. Hahn, K. Park, and M. Cho, J. Chem. Phys. **111**, 4121(1999).

[22] A. M. Moran, S. -M. Park, and S. Mukamel, J. Chem. Phys. **118**, 9971 (2003).

[23] T. Hayashi and S. Mukamel, J. Phys. Chem. A **107**, 9113 (2003).

[24] T. Hayashi, T. l. C. Jansen, W. Zhuang, and S. Mukamel, J. Phys. Chem. A **109**, 64 (2005).

[25] K. Tominaga and K. Yoshihara, Phys. Rev. Lett. **74**, 3061 (1995)

[26] K. Tominaga and K. Yoshihara, J. Chem. Phys. **104**, 4419 (1996).

[27] V. Astinov, K. J. Kubarych, C. J. Milne, and R. J. D. Miller, Chem. Phys. Lett. **327**,

334 (2000)

[28] K. J. Kubarych, C. L. Milne, S. Lin, V. Astinov, and R. J. D. Miller, J. Chem. Phys. **116**, 2016 (2002)

[29] K. J. Kubarych, C. J. Milne, and R. J. D. Miller, Chem. Phys. Lett. **369**, 635 (2003).

[30] A. Tokmakoff and G. R. Fleming, J. Chem. Phys. **106**, 2569 (1997).

[31] D. A. Blank, L. J. Kaufman, and G. R. Fleming, J. Chem. Phys. **113**, 771 (2000).

[32] L. J. Kaufman, D. A. Blank, and G. R. Fleming, J. Chem. Phys. **114**, 2312 (2001).

[33] L. J. Kaufman, J. Heo, L. D. Ziegler, and G. R. Fleming, Phys. Rev. Lett. **88**, 207402 (2002).

[34] J. Cao, S. Yang, and J. Wu, J. Chem. Phys. **116**, 3760 (2002).

[35] The supercooled liquids at $T = 95$, 120, and 160 K appear as metastable states. The detailed phase diagrams are shown in J. –P. Hansen and L. Verlet, Phys. Rev. **184**, 151 (1969); G. A. Vliegenthart, J. F. M. Lodge, and H. N. W. Lekkerkerker, Physica A **263**, 378 (1999).

[36] H. R. Schober and B. B. Laird, Phys. Rev. B **44**, 6746 (1991).

Chapter 4

TWO-DIMENSIONAL INFRARED SURFACE SPECTROSCOPY FOR CO ON CU(100): DETECTION OF INTERMOLECULAR COUPLING OF ADSORBATES

4-1. Introduction

The vibrational energy dissipation and intermolecular coupling of CO on various metal surfaces have attracted much attention and is well understood.[1] The CO stretching mode lifetime can be explained by an electron-hole (e-h) pair creation mechanism due to antibonding $2\pi^*$ orbital of the CO molecule.[2] The frustrated CO rotational mode have very short lifetimes dominated by the same mechanism.[3] [4] [5] Chemical shifts for the frustrated rotational mode are different for Cu(100) and Cu(111), [6] [7] which reflects the sensitivity of the adsorbate dynamics to the electronic structure of metal surfaces due to e-h pair creation. The stretching and frustrated rotational modes are anharmonically coupled to each other.[8] [9] At the same time, the CO frustrated rotational and translational modes are coupled.[10] These intermode couplings govern the dynamics of adsorbates on metal surface.

Dipole-dipole interactions play an important role on the geometry and lateral hopping of CO on Pd(100) and Pd(110).[11] [12] Researchers have tried to control lateral CO motions.[13] [14] [15] The lateral interactions make local ordering of adsorbates and prevent the formation of long range ordered structure at low coverage.[16] Particular attention has been paid to the overtone and combination bands of CO on Ru(001). Broadening of the CO

stretch overtone rapidly grows with temperature due to thermally activated decay of two-photon bound state into single phonon states.[17] Large anharmonicities due to lateral coupling lead to the formation of localized two-phonon bound states.[18] Thus, the investigation of the intermolecular couplings of CO adsorbed on metal surface is crucial for revealing the underlying mechanism of the surface dynamics.

In linear spectroscopy the couplings between intra- and inter-adsorbate interactions are measurable only in terms of chemical shifts. In addition, linear spectroscopy is unable to distinguish homogeneous broadening from inhomogeneous broadening.[19] [20] To overcome these limitations, multidimensional spectroscopic techniques have been proposed and carried out to obtain information on surface dynamics. Guyot-Sionnest combined the photon echo and sum-frequency generation (SFG) techniques [21] [22] to extract the homogeneous linewidth from the inhomogeneously broadened Si-H vibrations on Si(111) surface.[23] Cho proposed infrared-infrared-visible (IR-IR-VIS) SFG [24] and Bonn *et al.* determined the intermolecular coupling strength of dipole-coupled CO on Ru(001) using this SFG.[25] [26] However, IR-IR-VIS SFG is a third-order nonlinear optical process and is not surface-specific. Belabas and Joffre demonstrated two-dimensional (2D) VIS-IR spectroscopy in $AgGaS_2$.[27] Voelkmann *et al.* combined four-wave mixing with the second-harmonic generation to monitor the temporal evolution of photoexcited one- or two- photon coherence.[28]

In this study, we propose to apply 2D IR surface spectroscopy which utilizes the SFG of two independently tunable IR beams to an admixture of $C^{12}O^{16}$ and isotope labeled $C^{13}O^{16}$ on Cu(100). The pulse sequence and energy diagram of 2D IR surface spectroscopy is presented in Fig. 1 with those of 2D Raman spectroscopy. 2D IR surface spectroscopy has two independent time axes retaining the surface-specificity, and is related to the second-order response function,

$$R_{abc}^{(2)}(t_2,t_1)=\left(\frac{i}{\hbar}\right)^2\langle[[\mu_a(t_2),\mu_b(0)],\mu_c(-t_1)]\rangle, \tag{4.1}$$

where $\mu_a(t)$ is the dipole moment at time t in a direction.[19] [29] [30] [31] t_1 and t_2 are the time intervals between the first and second IR pulses and between the second pulse and the signal, respectively. Since the fifth-order Raman response function,

$$R^{(5)}_{abcdef}(t_2,t_1)=\left(\frac{i}{\hbar}\right)^2\left\langle\left[\left[\Pi_{ab}(t_2),\Pi_{cd}(0)\right],\Pi_{ef}(-t_1)\right]\right\rangle, \tag{4.2}$$

where $\Pi_{ab}(t)$ is the polarizability at time t in ab tensor, has the same form as the second-order IR response function Eq.(4.1), similar formulism and simulation strategies developed in 2D Raman spectroscopy [20] [32] [33] [34] [35] [36] [37] [38] [29] [40] [41] [42] [43] are applicable to 2D IR surface spectroscopy. We calculate 2D IR surface signals by means of molecular dynamics (MD) simulation based on the stability matrix formalism [33] [35] [37] [40] to investigate roles of anharmonic coupling.[34] In third-order IR spectra, ^{13}C and ^{18}O isotope substitution has been used to change the frequency [44] [45] [46] [47] [48] [49] and the cross peaks between two amide-I' modes were observed.[49] These suggest the possible detection of isotopic effects of adsorbates in 2D IR surface spectroscopy.

The aim of the present article is to explore a possibility of 2D IR surface spectroscopy to detect intermolecular anharmonic couplings between CO and isotopic CO stretching modes on Cu(100) at different temperatures. In Sec. 4.2 details of the MD simulation are explained. The temperature dependence of the first-order response functions of IR spectroscopy and the second order response functions of 2D IR surface spectroscopy are discussed in Sec. 4.3 and Sec. 4.4, respectively. Finally, concluding remarks are given in Sec. 4.5.

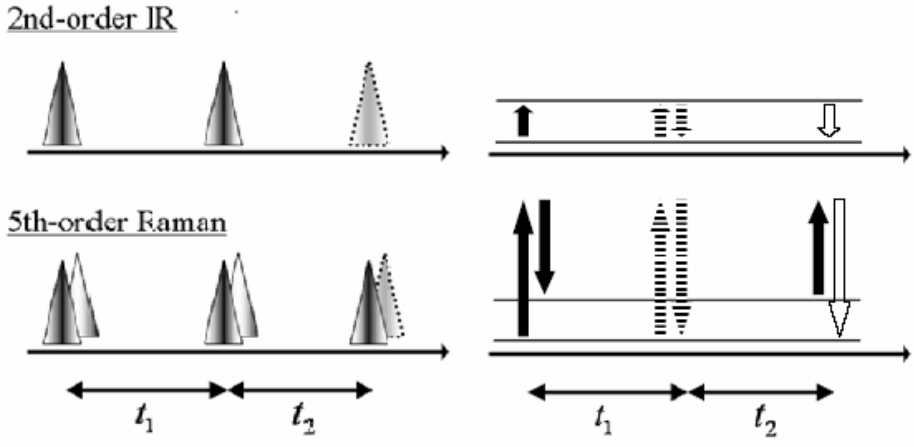

Figure 4.1. Pulse sequences (left) and typical energy diagrams (right) for 2nd-order IR surface spectroscopy and 5th-order Raman spectroscopy. Solid and dotted lines denote the transition of bra and ket vectors, respectively.

4-2. Molecular dynamics simulation

In 2D Raman spectroscopy researchers have calculated the classical limit of the fifth-order Raman response function

$$R^{(5)}_{abcdef}(t_2,t_1) = -\frac{1}{kT}\left\langle \{\Pi_{ab}(t_2),\Pi_{cd}(0)\}_{P.B.}\dot{\Pi}_{ef}(-t_1)\right\rangle, \tag{4.3}$$

where $\{\cdots\}_{P.B.}$, k, and T denote the Poisson bracket, boltzmann constant, and temperature, respectively.[33] [35] [36] [37] [38] [39] [40] [41] [42] [43] The response function Eq. (3) gives direct information on anharmonic dynamics [39] [43] and coherent dynamics through the stability matrix.[39] [40] Similarly, in 2D IR surface spectroscopy, it is necessary to calculate the classical limit of the second-order IR response function

$$\begin{aligned} R^{(2)}_{abc}(t_2,t_1) &= -\frac{1}{kT}\left\langle \{\mu_a(t_2),\mu_b(0)\}_{P.B.}\dot{\mu}_c(-t_1)\right\rangle \\ &= -\frac{1}{kT}\left\langle \sum_{ij}\frac{\partial\mu_a(t_2)}{\partial q_i(t_2)}\frac{\partial q_i(t_2)}{\partial p_j(0)}\frac{\partial\mu_b(0)}{\partial q_j(0)}\dot{\mu}_c(-t_1)\right\rangle \end{aligned} \tag{4.4}$$

in order to describe the surface dynamics and reveal the dynamical intermode correlation. We calculated the 2D surface IR signals by means of the MD simulation based on the stability matrix formalism, where calculation of stability matrix $\partial q_i(t_2)/\partial p_j(0)$ needs the $3N$ trajectories for one initial configuration, where N is the number of particles.

The following potentials were employed in our MD simulation; the Cu-Cu interaction potential developed by Wonchoba and Truhlar, [50] the Cu-C-O three-body potential and C-O intramolecular potential by Tully *et al.*, [5] and the CO-CO inter-adsorbate potential by van der Pol *et al.* [51] and Janssen *et al.*.[52] The inter-adsorbate potential included Van der Waals terms and electronic terms representing dipole-dipole, dipole-quadrupole, and quadrupole-quadrupole interactions. The effects of e-h pair creation was included as stochastic forces and frictions whose parameters are made by Tully *et al.*.[5] Similar MD simulations for CO on Cu surface have been carried out to investigate the desorption of CO from Cu(100) enhanced by neighbor CO molecules [53] and adsorption of CO on stepped surface of Cu(211).[54]

Our simulations were based on classical equations of motion for CO interacting with 4 surface layers with 16 Cu atoms in each layer. The bottom layer was rigid and interacted only

with the nearest layer. Since the CO intramolecular force was much stronger than the other forces, we employed the RESPA algorithm [55] summarized in the Appendix. The time evolution was carried out for $t_1 = t_2 = 1.6$ ps with $\Delta T = 1$ fs and $\Delta t = 0.1$ fs, where ΔT and Δt are the longer and shorter time steps defined in the RESPA. $t_1 = t_2 = 1.6$ ps is not enough to observe the linewidth of CO stretching mode in 1D plots or 2D maps, but is sufficient for the dynamical coupling between adsorbates. The Langevin equations were solved using Brunger-Brooks-Karplus algorithm.[56] To calculate the optical response, the dipole moment $\mu(t)$ was assumed to be

$$\mu(t) = \mu_0 + \mu_1 r(t), \tag{4.5}$$

where μ_0 and μ_1 denoted the permanent dipole moments and the first derivative of the dipole elements as the function of CO distance $r(t)$. By using *Gaussian03* package, the parameters $\mu_0 = 0.1326$ Debye and $\mu_1 = 9.098$ Debye Å^{-1} were determined from the optimized structure of free CO and OCCu with fixed 13 Cu atoms, respectively.[4] The optimized geometries and dipole moments were calculated at the B3LYP/6-31G(2d,p) level of the density functional theory.

The dipole moments for these high frequency modes are primarily determined by the intramolecular interactions. Therefore, the first derivatives of CO dipole moments with respect to Cu atoms degrees of freedom are negligible compared with those with respect to C and O atoms, making it unnecessary to calculate the stability matrix of Cu atoms.

In 2D Raman spectroscopy of pure liquids, non-equilibrium MD (NEMD) simulations are computationally less expensive than MD simulations based on the stability matrix formalism.[36] [42] This is because, for second-order IR or fifth-order Raman response functions, calculation of stability matrix requires $3N$ trajectories, while only 4 trajectories are needed in NEMD simulations.[42] However, when the simulations of multidimensional spectroscopy are directed to specific vibrational modes such as the CO vibrational mode of amide I in aqueous solution, [49] the above approximation requires only calculation of the stability matrix with respect to C and O atoms composing the CO vibrational mode, and the atoms around them if needed. It should be stressed that the above approximation may make the MD simulations based on the stability matrix formalism computationally less expensive than the NEMD.

The 2D signals were calculated by averaging over 1,500,000, 1,200,000, and 700,000 initial configurations for 60K, 100K, and 150K, respectively. Numerical convergence in time domain data was confirmed by checking the anti-symmetric integrated response functions which characterized the behavior of stability matrix [40]

$$A(t,t) = 2\langle \Pi(t)\{\Pi(0),\Pi(-t)\}_{P.B.}\rangle - \langle \Pi(0)\{\Pi(0),\Pi(-t)\}_{P.B.}\rangle - \langle \{\Pi(t),\Pi(0)\}_{P.B.}\Pi(0)\rangle \ . \quad (4.5)$$

The anti-symmetric integrated response functions for 60K, 100K, and 150K are shown in Fig. 4.2.

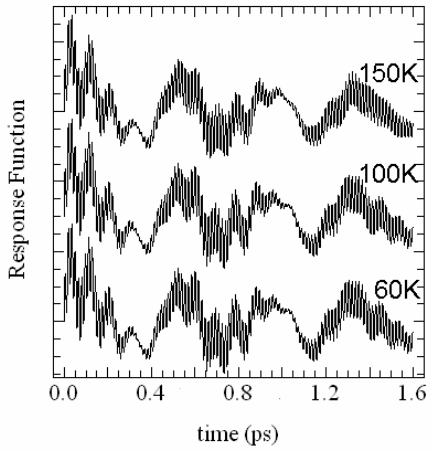

Figure 4.2. Anti-symmetric integrated response functions of second-order IR response functions at 60K, 100K, and 150K. Each plot is normalized at the maximum of the data.

4-3. Linear Response Function

The MD simulations of the linear response functions were carried out for four COs and isotopic COs on Cu(100) at 60K, 100K, and 150K. The spectra displayed in Fig. 4.3 show the CO stretching frequencies of CO and isotopic CO were $2179cm^{-1}$ and $2123cm^{-1}$ at 150K, respectively. The corresponding frequencies for one CO and isotopic CO on Cu(100) are $2175cm^{-1}$ and $2120cm^{-1}$. This shows blue shift due to the electronic interaction, in satisfactory agreement with the experiment.[6]

The peak positions are independent of temperature. Indeed temperature has influence on the linewidth in the experiment, but the linewidth is not precisely reproduced in our simulation as

stated in the previous section. Although the dynamics may be activated by increasing temperature, it has little effect on the CO stretching frequency. The spectra are not affected by the dynamics of neighbor adsorbates.

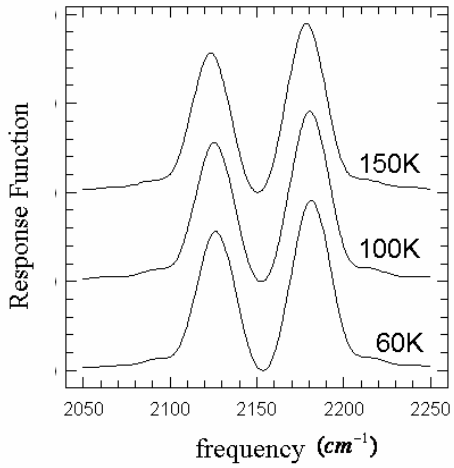

Figure 4.3. Linear spectra at 60K, 100K, and 150K. Each plot is normalized as the area is same at each temperature.

4-4. Two-dimensional Response Function

One of the merits of the 2D techniques is their capacity to identify signals corresponding to specific Liouville space pathways.[19] Here, we focus only on CO stretching modes. The double-sided Feynman diagrams corresponding to the peaks on the areas of the fundamental tone area $\left(2050cm^{-1} \le \omega_1 \le 2250cm^{-1}, 2050cm^{-1} \le \omega_2 \le 2250cm^{-1}\right)$ and overtone area $\left(2050cm^{-1} \le \omega_1 \le 2250cm^{-1}, 4100cm^{-1} \le \omega_2 \le 4500cm^{-1}\right)$ are sketched in Fig. 4.4(a) and (b), respectively.[30]

The calculated 2D signals in the fundamental tone area at different temperatures are depicted in Figs. 4.5. The main peaks are located at $(\omega_1, \omega_2) = \left(2123cm^{-1}, 2123cm^{-1}\right), \left(2123cm^{-1}, 2179cm^{-1}\right), \left(2179cm^{-1}, 2123cm^{-1}\right), \left(2179cm^{-1}, 2179cm^{-1}\right)$. Since the times $t_1 = t_2 = 1.6\,\text{ps}$ are shorter than the relaxation time of signals, we observe weak sidelobe peaks along $\omega_1 = 2123, 2179cm^{-1}$ and $\omega_2 = 2123, 2179cm^{-1}$.

The overtone transitions of a single oscillator such as $|0,0><0,0| \rightarrow |2,0><0,0|$ make a larger contribution to the diagonal peaks than the transitions due to the inter-adsorbate

couplings such as $|0,0><0,0| \rightarrow |1,1><0,0|$, where $|i,j>$ represents the combination of ith excited state of CO and jth excited state of isotopic CO. Thus, the insensitivity of diagonal peaks to temperature indicates that the potential anharmonicity with respect to single CO stretching mode $g_{111} \equiv \partial^3 V / \partial r_1^3$ is unchanged. The volumes of the cross peaks are at most about one tenth of those of the diagonal peaks.

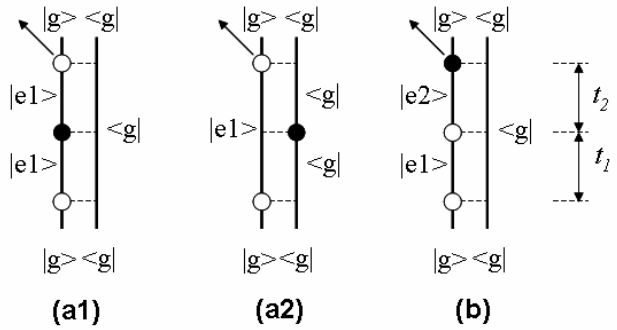

Figure 4.4. Double-sided Feynman diagrams of 2D IR surface response function in CO on Cu(100) corresponding to the signals (a) in the fundamental tone area and (b) in the overtone area. $|g>$, $|e1>$, and $|e2>$ represent ground state, one quanta excited states including $|1,0>$ and $|0,1>$, and two quanta excited states including $|2,0>$, $|1,1>$, and $|0,2>$, respectively. White and black circles show once and twice interactions between laser field and system.

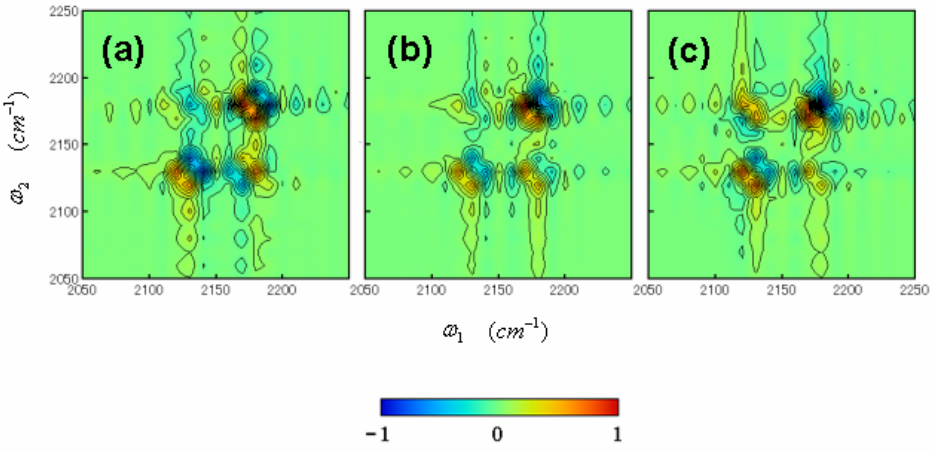

Figure 4.5. Imaginary parts of 2D signals of the fundamental tone at (a) 60K, (b) 100K, and (c) 150K. Each graph is normalized at maxima peaks.

The cross peaks representing anharmonic intermolecular couplings between CO and isotopic CO change significantly at 60K, 100K, and 150K. The intermolecular couplings are caused by intermolecular anharmonic potentials composed by different CO stretch modes.[24] At least, three primary causes for inter-adsorbate couplings are possible; induced dipole moments on Cu surface (e-h pair creation), the couplings through surface Cu atoms (phonon effect), and electronic interactions between CO and isotopic CO. The first mechanism is excluded in our simulation because the effect of e-h pair creation is expressed by the frictions and stochastic forces [5] and cannot produce the correlation between CO and isotopic CO. Therefore, we consider the latter two possibilities. To examine the second mechanism, we calculated the 2D signal at 150K by not allowing motion of the Cu atoms. The results shown in Fig. 4.6 resemble to the Fig. 4.5(c), which indicates that the phonon effect is not dominant for inter-adsorbate couplings. To evaluate the third mechanism, we calculated the 2D map at 150K with the electronic charges on CO to be zero, and illustrated it in Fig. 4.7. The cross peaks at $(\omega_1, \omega_2) = (2123cm^{-1}, 2179cm^{-1})$ in Fig. 4.7 are much weaker than those in Fig. 4.5, and the phase of the cross peaks at $(\omega_1, \omega_2) = (2179cm^{-1}, 2123cm^{-1})$ also changes between two figures. The inter-adsorbate interactions are primarily governed by electronic interactions which are about 10 times stronger than Van der Waals interactions. Therefore, the temperature dependence of the cross peaks may be attributed to electronic interactions.

Since the electric charges are fixed in our simulation, the electronic interaction strength depends on the distance between COs. In Fig. 4.8, we show the radial distribution functions (RDFs) of C-C, O-O, and Cu-Cu. The C-C and O-O RDFs similarly expand with temperature in contrast to the Cu-Cu RDF, indicating that temperature activates the frustrated rotational mode. The nonlinear dipole moments and anharmonicity of potentials give non-vanishing elements in the second-order IR response function as in the fifth-order Raman response function.[32] The nonlinearity, however, plays minor role on the second-order response function compared to the anharmonicity. In contrast, both give comparable contributions to the fifth-order Raman response function.[38] [29] [41] [30] Based on these arguments, we focused mainly on the electronic interactions through the dynamics of CO and its potential anharmonicity. Our model is simplified to extract the lateral dipole-dipole couplings on surface; the electric charges $-q$ on adsorbates and $+q$ on metal surface are set and the

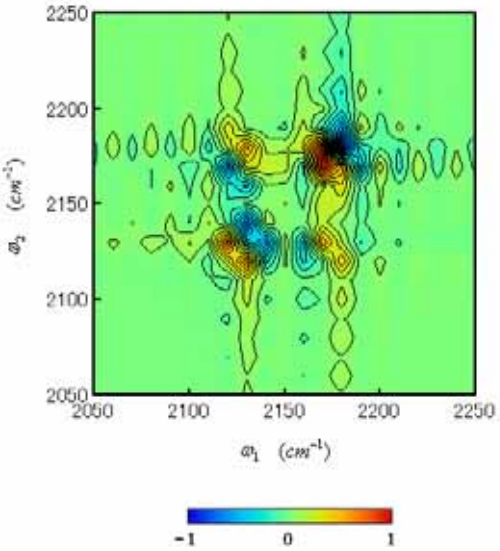

Figure 4.6. Imaginary parts of 2D signals of the the fundamental tone at 150K with Cu atoms fixed.

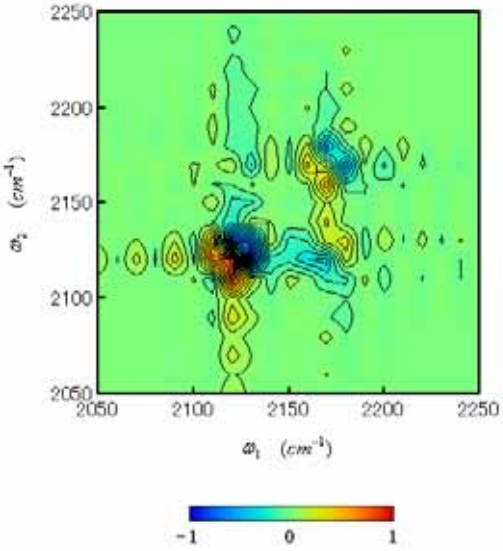

Figure 4.7. Imaginary parts of 2D signlas of fundamental tone at 150K without electronic interaction.

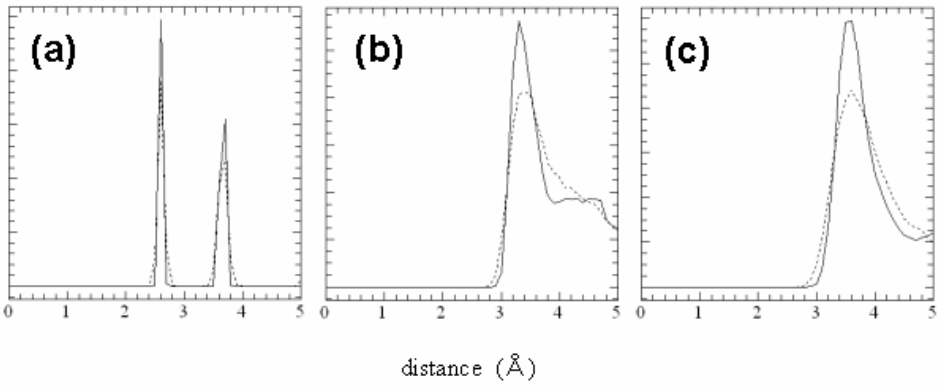

Figure 4.8. Radial distribution functions of (a) Cu-Cu, (b) C-C, and (c) O-O at 60K (solid) and 150K (dotted).

angles between dipole moments and vertical line, θ_1 and θ_2, are selected as variables (Fig. 4.9). The inter-adsorbate potential of a right side adosorbate is given by

$$V = \frac{1}{4\pi\varepsilon}\frac{q^2}{\left(\left(R - r_1\sin\theta_1 + r_2\sin\theta_2\right)^2 + \left(r_1\cos\theta_1 - r_2\cos\theta_2\right)^2\right)^{1/2}} - \frac{1}{4\pi\varepsilon}\frac{q^2}{\left(\left(R + r_2\sin\theta_2\right)^2 + \left(r_2\cos\theta_2\right)^2\right)^{1/2}}, \quad (4.7)$$

where R is the distance between surface atoms and r_i is the distance between the ith adsorbate and the corresponding surface atom. The strengths of the cross peaks are proportional to the potential anharmonicity for different normal modes $g_{122} \equiv \partial^3 V / \partial r_1 \partial r_2^{\,2}$. [24] [32] [34] We plot g_{122} in Fig. 4.10 as the functions of θ_1 and θ_2 with $R = 3.6A$, $r_1 = r_2 = 1.9A$, and $r_1 q = 1 Debye$ for simplicity. It is found that g_{122} increases monotonously as $\theta_1 - \theta_2$ increases. It is found that g_{122} increases monotonously as $\theta_1 - \theta_2$ increases. The $\theta_1 - \theta_2$ distribution for all adsorbates is shown in Fig. 4.11. This indicates that the rotational dynamics of adsorbates becomes active for higher temperature, which leads the wider $\theta_1 - \theta_2$ distribution. The wider $\theta_1 - \theta_2$ distribution increases the anharmonicity of potentials g_{122} and changes the phase of the cross peaks followed by Fig. 4.10.

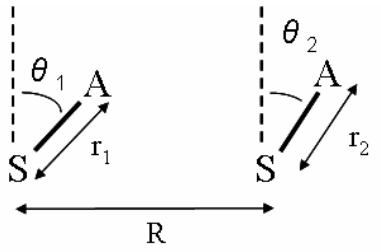

Figure 4.9. The model with two dipole moments. A and S denote the adsorbate and surface atoms.

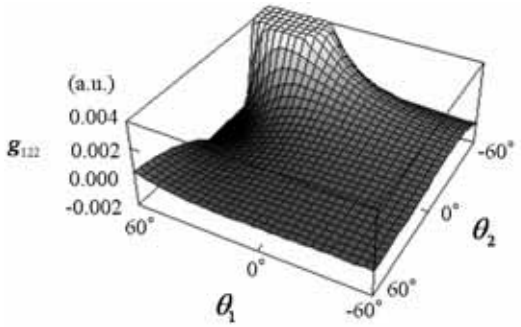

Figure 4.10. Anharmonicity of potential g_{122} as functions of θ_1 and θ_2.

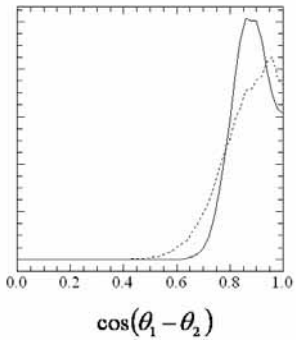

Figure 4.11. $\cos(\theta_1-\theta_2)$ distribution when Cu-Cu distance is less than 3.8A.

The distributions at 60K and 150K denote solid and dotted lines, respectively.

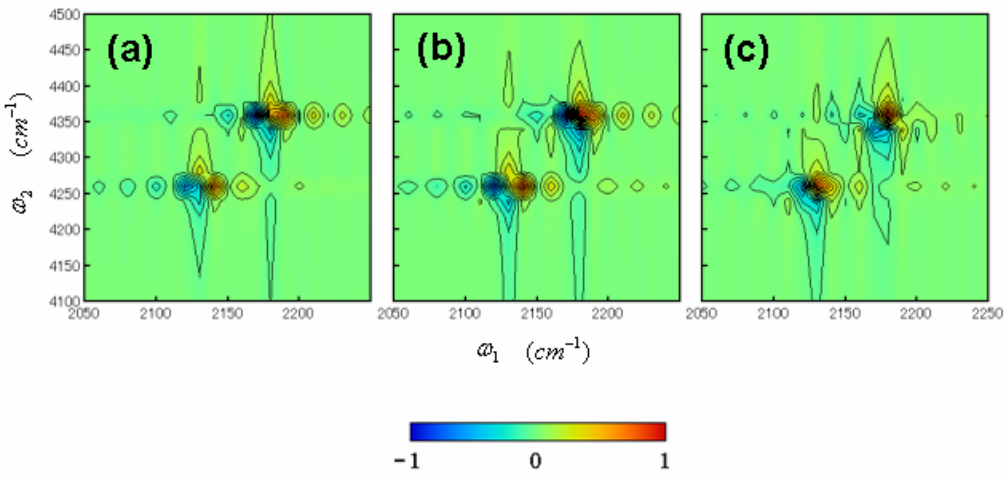

Figure 4.12. Imaginary parts of 2D signals of the overtone at (a) 60K, (b) 100K, and (c) 150K.

Each graph is normalized at maxima peaks.

Finally, the calculated 2D signals in the overtone area at different temperatures are shown in Figs. 4.12. When Figs. 4.5 and 4.12 are compared, we can find that the cross peaks of Fig. 4.11 are much smaller than those of Fig. 4.5. This can be explained by the double-sided Feynman diagrams in Fig. 4.4. The cross peaks in the fundamental tone area arise from, for example, the optical process $|0,0><0,0|\rightarrow|1,0><0,0|\rightarrow|0,1><0,0|\rightarrow|0,0><0,0|$ in Feynman diagram Fig. 4.4(a1). Similarly, the cross peaks in the overtone area arise from, for example, the process $|0,0><0,0|\rightarrow|1,0><0,0|\rightarrow|1,1><0,0|\rightarrow|0,0><0,0|$ in Fig. 4.4(b).

Since the one quantum process $|1,0><0,0|\rightarrow|1,1><0,0|$ and two quanta processes, $|1,0><0,0|\rightarrow|0,1><0,0|$ and $|1,1><0,0|\rightarrow|0,0><0,0|$, require the couplings between CO and isotoped CO and have much less transition dipole moment than the one quantum processes, $|0,0><0,0|\rightarrow|1,0><0,0|$ and $|0,1><0,0|\rightarrow|0,0><0,0|$, the cross peaks in the fundamental tone area are bigger than those in the overtone area. Moreover, the diagonal peaks in the overtone area have opposite signs as those in the fundamental tone area. As was shown in the fifth-order Raman spectroscopy, [41] the peak intensities of the signals in frequency domain 2D maps are determined by the interplay between the nonlinear coordinate dependence of dipole moments (NL) and the anharmonicity if potential (AN); NL+AN contributes to the diagonal peaks in the fundamental tone area, while NL-AN contributes to the diagonal peaks in the overtone area. Since the contributions of NL to 2D signals are much smaller than those of AN, the signs of the diagonal peaks in the fundamental tone and overtone areas become positive and negative corresponding to the contributions AN and –AN, respectively.

4-5. Concluding Remarks

We carried out the MD simulation for CO on Cu(100) to calculate the signals of 2D IR surface spectroscopy for various temperatures. Our MD simulation was based on the stability matrix formalism and e-h pair creation was included as a stochastic process. When temperatures were set to be 60K, 100K, and 150K, the cross peaks were significantly changed in the fundamental tone areas of 2D frequency domain maps, while the appreciable difference could not be found in linear response functions. Comparison of the signals from the MD simulations without electronic interactions and with surface Cu atoms fixed indicated that the electronic interactions were the primary cause of the temperature dependence of the cross peaks. To explore this point, we employed the simple model with two dipole moments whose configurations were characterized by the angles between dipole moments and vertical line θ_1 and θ_2. It was found that the increase of $\theta_1 - \theta_2$ changed the anharmonicity from negative to positive signs. In fact, wider $\theta_1 - \theta_2$ distribution with higher temperature was observed in our simulation. The frustrated rotational mode activated by increasing temperature changed

the anharmonicity of potentials and, consequently, the phase of cross peaks.

We further compared the signals in the overtone area with in the fundamental tone area. The cross peaks in the overtone area were much smaller than those in the fundamental tone area. This was because the couplings between CO and isotoped CO were required twice in the optical process corresponding to the signals in the overtone area, while there was one coupling in the optical process in the fundamental tone area. Moreover the phases of the diagonal peaks were changed between in the fundamental tone area and in the overtone area. This was explained from our previous study of 2D Raman spectroscopy, the anharmonicity of potential with respect to the single CO stretching mode gave positive and negative contribution to the fundamental tone and the overtone, respectively.

Finally, we make the following two points. First, the e-h pair creation mechanism plays a major role in surface dynamics such as pure dephasing on metal surface.[57] and theoretical descriptions of e-h pair creation are well tested.[58] [59] Although the effect of e-h pair creation was treated by using the friction and stochastic forces in this study, it is challenging to simulate the influence of e-h pair creation on the inter-adosorbate couplings. Second, some studies have shown the capacity of 2D IR spectroscopy to reveal the intermolecular interactions by probing the intramolecular interactions. [60] [61] [62] [63] For example, Zheng *et al.* probed the equilibrium dynamics of phenol complexation to benzene in a benzene-carbon tetrachloride solvent mixture, [60] [61] and Cowan *et al.* investigated into the loss of memory of persistent correlations in water structure. [62]. In this study the temperature dependence of the inter-adsorbate coupling was discussed by observing the cross peaks of the CO stretch. This study demonstrated the same ability of the multidimensional IR spectroscopies to provide similar information on surfaces as well as in the bulk.

4-6. Appendix: Summary of RESPA

The RESPA was introduced to lower the computation cost of integrating the equations of motion by separating all forces into short and long range types, F_s and F_l.[55] These forces are integrated with different time steps. In one dimensional system, the Liouville operator L can be rewritten as

$$iL = iL_K + iL_{Vs} + iL_{Vl}, \tag{4.7}$$

where

$$iL_K = \dot{x}\frac{\partial}{\partial x}, \tag{4.8}$$

$$iL_{Vs} = F_s(x)\frac{\partial}{\partial p}, \tag{4.9}$$

and

$$iL_{Vl} = F_l(x)\frac{\partial}{\partial p}. \tag{4.10}$$

The propagator can then be written

$$e^{iL\Delta T} = e^{iL_{Vl}(\Delta t/2)}\left[e^{iL_K(\Delta t/2)}e^{iL_{Vs}\Delta t}e^{iL_K(\Delta t/2)} + O\left(\Delta t^3\right)\right]^n e^{iL_{Vl}(\Delta t/2)} + O\left(\Delta T^3\right), \tag{4.11}$$

where $\Delta t = \Delta T/n$.

In our system, the force by the CO intramolecular potential corresponds to F_s, while all other forces are classified into F_l. The Liouville operator of the kinetic part can be decomposed into fast and slow motion parts corresponding to F_s and F_l, respectively.

$$iL_K = iL_{Ks} + iL_{Kl}. \tag{4.12}$$

Note that L_{Ks} is dependent on the degrees of freedom of C and O atoms, while L_{Kl} includes the degrees of freedom of all atoms. Since Cu atoms are independent of F_s, the time evolution of Cu atoms can be extracted from the iteration with smaller time step. Thus, we get

$$\begin{aligned} e^{iL\Delta T} &= e^{iL_{Vl}(\Delta T/2)}\left[e^{i(L_{Kl}+L_{Ks}+L_{Vs})\Delta t}\right]^n e^{iL_{Vl}(\Delta T/2)} + O\left(\Delta T^3\right) \\ &= e^{iL_{Vl}(\Delta T/2)}\left[e^{iL_{Ks}(\Delta t/2)}e^{iL_{Vs}\Delta t}e^{iL_{Ks}(\Delta t/2)} + O\left(\Delta t^3\right)\right]^n e^{iL_{Kl}\Delta T}e^{iL_{Vl}(\Delta T/2)} + O\left(\Delta T^3\right). \end{aligned} \tag{4.13}$$

Eq. (4.13) avoiding n times time evolution with respect to the position of Cu atoms compared with the original RESPA (4.11).

The increase of the atoms independent of the short range forces accelerates the efficiency of Eq. (4.13). The methodology is useful in the MD simulations ranging from the surface dynamics to the molecules in the solution in which the solute molecules are treated as rigid bodies and interacts with the solute molecules. We explain this methodology using the velocity Verlet algorism which is an example of a second order symplectic integrator. This methodology is more important for the higher order symplectic integrator method.

4-7. Reference

[1] J. C. Tully, Annu. Rev. Phys. Chem. **51**, 153 (2000).

[2] B. N. J. Persson and M. Persson, Solid State Commun. **36**, 175 (1980).

[3] M. H-. Gordon and J. C. Tully, J. Chem. Phys. **96**, 3939 (1992).

[4] M. H-. Gordon and J. C. Tully, Phys. Rev. B **46**, 1853 (1992).

[5] J. C. Tully, M. Gomez, and M. H-. Gordon, J. Vac. Sci. Technol. A **11**, 1914 (1993).

[6] C. J. Hirschmugel, G. P. Williams, F. M. Hoffmann, and Y. J. Chabal, Phys. Rev. Lett. **65**, 480 (1990).

[7] C. J. Hirschmugel and G. P. Williams, Phys. Rev. B **52**, 14177 (1995).

[8] J. P. Culver, M. Li, L. G. Jahn, R. M. Hochsrasser, and A. G. Todh, Chem. Phys. Lett. **214**, 431 (1993).

[9] T. A. Germer, J. C. Stephenson, E. J. Heilweil, and R. R, Cavanagh, J. Chem. Phys. **101**, 1704 (1994).

[10] A. P. Graham, F. Hofmann, J. P. Toennies, G. P. Williams, C. J. Hirschmugl, and J. Ellis J. Chem. Phys. **108**, 7825 (1998).

[11] H. Kato, M. Kawai, and J. Yoshinobu, Phys. Rev. Lett. **82**, 1899 (1999).

[12] J. Yoshinobu, N. Takagi, and M. Kawai, Phys. Rev. B **49**, 16670 (1994).

[13] H. J. Lee and W. Ho, Science **286**, 1719 (1999).

[14] .T. Komeda, Y. Kim, M. Kawai, B. N. J. Persson, and H. Ueba, Science **295**, 2055 (2002).

[15] L. Bartels, F. Wang, D. Moller, E. Knoesel, and T. F. Heinz, Science **305**, 648 (2004).

[16] E. Borguet and H.L. Dai, J. Phys. Chem. B **109**, 8509 (2005).

[17] P. Jakob, Phys. Rev. Lett. **77**, 4229 (1996).

[18] P. Jakob and B. N. J. Persson, J. Chem. Phys. **109**, 8641 (1998).

[19] S. Mukamel, *Principles of Nonlinear Optical Spectroscopy* (Oxford University Press, New York, 1995).

[20] Y. Tanimura and S. Mukamel, J. Chem. Phys. **99**, 9496 (1993).

[21] Y. R. Shen, *The Principles of Nonlinear Optics* (Wiley-Interscience, New York, 1984).

[22] X. D. Zhu and Y. R. Shen, Appl. Phys. B **50**, 535 (1990).

[23] P. Guyot-Sionnest, Phys. Rev. Lett. **66**, 1489 (1991).

[24] M. Cho, Phys. Rev. A **61**, 023406 (2000).

[25] M. Bonn, C. Hess, J. H. Miners, T. F. Heinz, H. J. Bakker, and M. Cho, Phys. Rev. Lett. **86**, 1566 (2001).

[26] M. H. Cho, C. Hess, and M. Bonn, Phys. Rev. B **65**, 205423 (2002).

[27] N. Belabas and M. Joffre, Opt. Lett. **27**, 2043 (2002).

[28] C. Voelkmann, M. Reichelt, T. Meier, S. W. Koch, and U. Hofer, Phys. Rev. Lett. **92**, 127405 (2004).

[29] M. Cho, J. Chem. Phys. **112**, 9978 (2000).

[30] K. Okumura and Y. Tanimura, J. Phys. Chem. A **107**, 8092 (2003).

[31] R. Venkatramani and S. Mukamel, J. Phys. Chem. B **109**, 8132 (2005).

[32] K. Okumura and Y. Tanimura, J. Chem. Phys. **107**, 2267 (1997).

[33] S. Mukamel, V. Khidekel, and V. Chernyak, Phys. Rev. E **53**, R1 (1996).

[34] S. Saito and I. Ohmine, J. Chem. Phys. **108**, 240 (1998).

[35] A. Ma and R. M. Stratt, Phys. Rev. Lett. **85**, 1004 (2000).

[36] T.l.C. Jansen, J.G. Snijders, and K. Duppen, J. Chem. Phys. **113**, 307 (2000).

[37] S. Saito and I. Ohmine, Phys. Rev. Lett. **88**, 207401 (2002).

[38] A. Ma and R.M. Stratt, J. Chem. Phys. **116**, 4972 (2002).

[39] S. Saito and I. Ohmine, J. Chem. Phys. **119**, 9073 (2003).

[40] Y. Nagata and Y. Tanimura, J. Chem. Phys. **124**, 024508 (2006).

[41] Y. Nagata, T. Hasegawa, and Y. Tanimura, J. Chem. Phys. **124**, 194504 (2006).

[42] T. Hasegawa and Y. Tanimura, J. Chem. Phys. **125**, 074512 (2006).

[43] S. Saito and I. Ohime, J. Chem. Phys. **125**, 084506 (2006).

[44] S. Woutersen and P. Hamm, J. Chem. Phys. **114**, 2727 (2001).

[45] J. Bredenbeck and P. Hamm, J. Chem. Phys. **119**, 1569 (2003).

[46] C. Fang, J. Wang, A. K. Charnley, W. Barber-Armstrong, A. B. Smith, S. M. Decatur, and R. M. Hochstrasser, Chem. Phys. Lett. **382**, 586 (2003).

[47] P. Mukherjee, A. T. Krummel, E. C. Fulmer, I. Kass, I. T. Arkin, and M. T. Zanni, J. Chem. Phys. **120**, 10215 (2004).

[48] C. Fang, J. Wang, Y. S. Kim, A. K. Charnley, W. Barber-Armstrong, A. B. Smith, S.

M. Decatur, and R. M. Hochstrasser, J. Phys. Chem. B **108**, 10415 (2004).

[49] Y. S. Kim, J. Wang, and R. M. Hochstrasser, J. Phys. Chem. B, **109**, 7511 (2005).

[50] S. E. Wonchoba, and D. G. Truhlar, J. Chem. Phys. **99**, 9637 (1993).

[51] A. van der Pol, A. van der Avoird, and P. E. S. Wormer, J. Chem. Phys. **92**, 7498 (1990).

[52] W. B. J. M. Janssen, J. Michiels, and A. van der Avoird, J. Chem. Phys. **94**, 8402 (1991).

[53] C. Springer, and M. H-. Gordon, Chem. Phys. **205**, 73 (1996).

[54] M. -C. Marinica, H. Le Rouzo, and G. Raseev, Surf. Sci. **542**, 1 (2003).

[55] M. Tuckerman, B. J. Berne, and G. J. Martyna, J. Chem. Phys. **97**, 1990 (1992).

[56] A. Brunger, C. L. Brooks, and M. Karplus, Chem. Phys. Lett. **105**, 495 (1984).

[57] K. Watanabe, N. Takagi, and Y. Matsumoto, Phys. Rev. Lett. **92**, 057401 (2004).

[58] F. Weik, A. Demeijere, and E. Hasselbrink, J. Chem. Phys. **99**, 682 (1993).

[59] H. Nakamura and K. Yamashita, J. Chem. Phys. **122**, 194706 (2005).

[60] J. R. Zheng, K. Kwak, J. Asbury, Z. Chen, I. R. Piletic, and M. D. Fayer, Science **309**, 1338 (2005).

[61] K, Kwak, C. Lee, Y. Jung, J. Han, K. Kwak, J. R. Zheng, M. D. Fayer, and M. Cho, J. Chem. Phys. **125**, 244508 (2006).

[62] M. L. Cowan, B. D. Bruner, N. Huse, J. R. Dwyer, B. Chung, E. T. J. Nibbering, T. Elsaesser, and R. J. D. Miller, Nature **434**, 199 (2005).

[63] J. D. Eaves, J. J. Loparo, C. J. Fecko, S. T. Roberts, A. Tokmakoff, and P. L. Geissler, Pro. Nat. Aca. Sci. **102**, 13019 (2005).

Chapter 5

CONCLUSION

5-1. Quantitative Analyses Beyond Qualitative

Over ten years passed since 2D Raman spectroscopy was proposed theoretically, [1] and some experimental successes were reported.[2] [3] [4] [5] By using MD simulations the 2D Raman signals were calculated in Xe, [6] [7] CS_2, [7] [8] water, [7] [9] [10] benzene, [11] and soft core system.[12] When these experimental and simulation results were discussed, one usually employed oversimplified models such as the Brownian oscillator model.[13] The discussions and analyses by using these models were qualitative rather than quantitative. Quantitative analyses beyond qualitative shall be required as the next stage of 2D Raman spectroscopy to insight into the details of molecular dynamics.

Without navigation tools for 2D maps, it is difficult to compare experimental data or simulation data with each other. For example, although we can obtain some information such as peak positions and direction of ridges from the 2D maps, we cannot extract any information on dynamics as long as the underlying mechanisms of these features are not revealed. Tthe projection of the 2D maps onto the 1D plots without loss of important information which characterizes the fifth-order Raman response function is one of the practical ways to analyze the 2D signals. How we project the 2D maps onto 1D plots depends on what we want to investigate. In this thesis, we showed two examples: if we want to know the role of the stability matrix, analyzing the antisymmetric integrated response function is the best approach.[12] If you want to know the ratio between anharmonicity contributions and nonlinear polarizability which are the main sources of the 2D Raman signal, analyzing the 2D frequency-domain map is the best way.[14] Note that the former approach can extract more dynamical information than the latter.

In chapter 2, we applied these methods to the soft core system and found that even in femtosecond order ultrafast region 2D Raman signals can capture the difference between solid

and liquid phases to which the linear Raman spectra are not sensitive. This indicates that 2D Raman spectroscopy has a possibility to investigate the detailed molecular dynamics and structures near critical points which cannot be observable in linear Raman spectroscopy.

The sensitivity of 2D Raman spectroscopy arises from the anharmonicity of potentials and nonlinear coordinate dependence of polarizability because harmonic dynamics with linear polarizability has no contribution to the 2D Raman signals.[1] [13] In chapter 3, [14] we derived the expressions of 2D Raman signals for Morse potential in the Brownian oscillator model using the perturbative solution of equation of motions. If the Fourier transformations of 2D Raman signals are carried out, the peaks shall be located along $\omega_1 = \omega_2$ and $\omega_1 = \omega_2/2$ axes in a 2D frequency domain map. By evaluating the volume of each peak, we can measure the ratio between the anharmonicity of potentials and nonlinear polarizability contributions through Eq. (3.24).

When Fourier transformation was performed for the 2D time domain data of soft core system, we found there were two peaks from the localized and delocalized modes. By measuring the spectral volume in the 2D maps in frequency domain, only the nonlinearity contribution of the localized mode showed dramatic change between liquid and solid phases, while other nonlinearity and anharmonicity contributions were continuously changed between them. This result indicates that the nonlinear polarizability is sensitive to the change in molecular structure and dynamics. We found that only localized mode of the soft core potential system varied between solid and liquid phases.

5-2. Application of the multi-dimensional spectroscopy to surface spectroscopy

Both from the experimental and theoretical points of view, it is natural to develop multidimensional surface spectroscopy in the following reasons. From the experimental point of view, the information of dynamical inter- and intra-adsorbate coupling is important to reveal the underlying surface dynamics. The inter-adsorbate interactions, however, appear as chemical shifts in linear spectroscopy, which does not represent the intermode couplings. Here, multidimensional spectroscopies for bulk system such as 2D IR and Raman

spectroscopies have given us the information on direct anharmonic couplings between different modes and anharmonic dynamics. To investigate the details of inter-adsorbate couplings on surface, 2D techniques should be applied to surface spectroscopy. From the theoretical point of view, the second-order IR response function has the same expression as the fifth-order Raman response function, which indicates that similar formalisms or discussions developed in 2D Raman spectroscopy are applicable to 2D IR surface spectroscopy. According to the previous chapters on fifth-order Raman spectroscopy, we can separate homogeneous broadening from inhomogeneous broaded spectra, [1] we can obtain information on the intermode couplings, [15] and we can extract the contributions of nonlinear coordinate dependence of dipole moments and anharmonicity of potentials with respect to normal mode by using 2D Raman spectroscopy.[13] The information which is expected to be obtained in 2D IR surface spectroscopy is also important for clarifying the underlying surface dynamics.

Indeed the pioneering researches have targeted at higher-order spectroscopies to detect the details of surface dynamics by some groups as stated in Sec. 4-1, but these experiments have not explored the merits of 2D technique such as the detection of intermode couplings. Here, I considered the detection of intermolecular coupling between adsorbates on metal surface by using 2D IR surface spectroscopy for demonstration.[16] I applied it to an admixture of CO and isotoped CO on Cu(100) by means of MD simulations based on the stability matrix formalism.

The 2D profiles of the signals in frequency domain showed both diagonal and cross peaks. The former peaks mainly arose from the overtones of the CO and isotoped CO, while the latter represented the couplings between those. As temperature increased, the phases of cross peaks in a second-order infrared response function changed significantly, while those of diagonal peaks are unchanged. We showed that the phase shifts were originated from anharmonicity of potentials due to the electronic interaction between adsorbates. Using a model with two-dipole moments, we found that the frustrated rotational mode activated with temperature had effects on the anharmonicity.

These results indicate that 2D IR surface spectroscopy reveals the anharmonic couplings between adsorbates and surface atoms or between adsorbates which can not be observed in

linear spectroscopy.

5-3. Reference

[1] Y. Tanimura and S. Mukamel, J. Chem. Phys. **99**, 9496 (1993).

[2] V. Astinov, K. J. Kubarych, C. J. Milne and, R. J. D. Miller, Chem. Phys. Lett. **327**, 34 (2000).

[3] K. J. Kubarych, C. L. Milne, S. Lin, V. Astinov, and R. J. D. Miller, J. Chem. Phys. **116**, 2016 (2002).

[4] C. L. Milne, Y. L. Li, T. l. C. Jansen, L. Huang, and R. J. D. Miller, J. Phys. Chem. B **110**, 19867 (2006).

[5] L. J. Kaufman, J. Heo, L. D. Ziegler, and G. R. Fleming, Phys. Rev. Lett. **88**, 207402 (2002).

[6] A. Ma and R. M. Stratt, Phys. Rev. Lett. **85**, 1004 (2000).

[7] T. Hasegawa and Y. Tanimura, J. Chem. Phys. **125**, 074512 (2006).

[8] S. Saito and I. Ohmine, Phys. Rev. Lett. **88**, 207401 (2002).

[9] S. Saito and I. Ohmine, J. Chem. Phys. **119**, 9073 (2003).

[10] S. Saito and I. Ohmine, J. Chem. Phys. **125**, 084506 (2006).

[11] C. L. Milne, Y. L. Li, T. l. C. Jansen, L. Huang, and R. J. D. Miller, J. Phys. Chem. B **110**, 19867 (2006).

[12] Y. Nagata and Y. Tanimura, J. Chem. Phys. **124**, 024508 (2006).

[13] K. Okumura and Y. Tanimura, J. Chem. Phys.**106**, 1687 (1997).

[14] Y. Nagata, T. Hasegawa, and Y. Tanimura, J. Chem. Phys., **124**, 194504 (2006).

[15] S. Saito and I. Ohmine, J. Chem. Phys. **108**, 240 (1998).

[16] Y. Nagata, Y. Tanimura, and S. Mukamel, J. Chem. Phys. *submitted* (2007).